Study of spin-torque nano-oscillators driven by nonlocal spin injection

Master thesis

Boris Divinskiy, WWU Münster
Student no. 423637

Supervisors
Prof. Dr. Sergej O. Demokritov
Dr. Vladislav E. Demidov

Münster, March 2016

Westfälische
Wilhelms-Universität
Münster

1. Gutachter: Prof. Dr. S. O. Demokritov
2. Gutachter: Dr. V. E. Demidov

Zusammenfassung

Die Nutzung reiner Spinströme, erzeugt entweder durch den Spin-Hall-Effekt (SHE) oder nichtlokale Spininjektion (NLSI), eröffnet neue Perspektiven für neue Technologien auf der Grundlage des Elektronspin Freiheitsgrades, wie Spintronik und Magnonik. Beispielsweise können unter Verwendung von reinen Spinströmen in nanoskaligen magnetischen Strukturen durch die Spin-Drehmomentübertragung (STT) effizient kohärente Magnetisierungsdynamiken angeregt werden. Diese neue Methode der Erzeugung von Mikrowellenoszillationen hat in den letzten Jahren viel Aufmerksamkeit auf sich gezogen. Allerdings wurden in den meisten Experimenten SHE-basierte Systeme untersucht und es ist noch wenig über die strominduzierte Dynamik NLSI basierter Strukturen bekannt.

Diese Arbeit behandelt magnetische Nanooszillatoren, die durch reine Spinströme unter Ausnutzung des nichtlokalen Spininjektions Mechanismus angetrieben werden. Zuerst diskutieren wir die Joule-Erwärmungseffekte in den Geräten und demonstrieren, dass sich diese im Vergleich zu SHE-basierten Oszillatoren minimiert. Zweitens untersuchen wir die spektralen Eigenschaften der strominduzierten Magnetisierungsdynamik und zeigen, dass die Systeme hoch kohärente Schwingungen bei Raumtemperatur aufweisen. Schliesslich zeigen wir, wie die nach dem NLSI Mechanismus erzeugte, reine Spinströme genutzt werden können, um sich in einer vorgegebenen Richtung ausbreitende Spinwellen anzuregen. Alle diskutierten Merkmale zeigen signifikantes Potenzial der nichtlokalen Oszillatoren für Anwendungen in der Elektronik der nächsten Generation.

Abstract

Utilization of pure spin currents, produced either by the spin-Hall effect (SHE) or by the nonlocal spin injection (NLSI), opens new perspectives for the emerging technologies based on the electron's spin degree of freedom, such as spintronics and magnonics. For example, by using pure spin currents one can efficiently excite coherent magnetization dynamics in nanosize magnetic structures by means of the spin-transfer torque (STT) effect. This new method of generation of microwave oscillations has been drawing a lot of attention of researches for the last several years. However, in most experiments SHE-based systems have been studied, and still little is known about the current-induced dynamics in NLSI-based structures.

This thesis is devoted to a study of magnetic nano-oscillators driven by pure spin currents produced by the nonlocal spin injection mechanism. At first, we discuss the Joule heating effects in the devices and demonstrate that they are minimized in comparison with SHE-based oscillators. Secondly, we investigate the spectral properties of the current-induced magnetization dynamics and show that the devices exhibit highly-coherent oscillations at room temperature. Finally, we demonstrate how pure spin currents generated by the NLSI mechanism can be used to excite directionally propagating spin waves. All discussed features show significant potential of the nonlocal oscillators for applications in the future-generation electronics.

Contents

1 Introduction **1**

2 Basic Theory **3**
2.1 Equations of magnetization dynamics 3
2.2 Spin-transfer torque effect 5
2.3 Magnetization auto-oscillations 6
2.4 Pure spin currents 9

3 Methods **12**
3.1 Micro-focus Brillouin light scattering spectroscopy 12
3.2 Micromagnetic simulations 14

4 Joule heating in nano-oscillators **16**
4.1 SHE-based oscillator 16
4.2 NLSI-based oscillator 19
4.3 Conclusions 21

5 Spectral linewidth of nano-oscillators driven by nonlocal spin injection **23**
5.1 BLS measurements 24
5.2 Electronic measurements 26
5.3 Conclusions 29

6 Excitation of propagating spin waves by nonlocal spin injection **31**
6.1 Waveguide optimization 32
6.2 Experiment 36
6.3 Micromagnetic simulations 40
6.4 Conclusions 44

7 General conclusions and outlook **45**

Tables with acronyms and symbols

Table 1: Commonly used acronyms

Notation in text	Meaning
Py	Permaloy = $Ni_{80}Fe_{20}$
CoFe	$Co_{70}Fe_{30}$
SHE	Spin-Hall effect
NLSI	Non-local spin injection
STT	Spin-transfer torque
STNO	Spin-torque nano-oscillator
BLS	Brillouin light scattering
FMR	Ferromagnetic resonance

Table 2: Commonly used symbols

Notation in text	Meaning
$\mathbf{H}_0$	External magnetic field
$\mathbf{H}_{dem}$	Demagnetizing field
$\mathbf{H}_{int}$	Internal field
$\mathbf{M}$	Magnetization
M_0	Saturation magnetization
I	Current
I_c	Critical current
f	Frequency
Δf	FWHM

Chapter 1

Introduction

Magnonics is a young and promising field of modern magnetism which main aim is to investigate the behavior of spin waves in magnetic nanostructures and to turn the obtained knowledge into technical applications [1, 2, 3]. Spin waves itself were introduced by Felix Bloch in 1930 to explain the temperature dependence of the saturation magnetization at low temperatures [4]. From a classical point of view, a spin wave can be represented as a phase-coherent precession of magnetic moments localized at crystal lattice sites [5, 6]. At the same time, one can consider spin waves as collective excitations in magnetically ordered systems and describe them as a gas of weakly interacting quisiparticles, magnons [7, 8].

The efficient excitation of spin waves is an important issues in magnonics because it determines the power consumption and error rates of magnonic devices [1]. The classical method is the inductive technique, when an alternating electrical current applied to a microwave antenna. The signal produces an oscillating Oersted field, which excites magnetization precessions in a magnetic sample [9, 10, 11]. Despite the method has a few shortcomings [11], it is still widely used in experiments. But in 1996 almost simultaneously Slonczewski [12] and Berger [13] theoretically discovered a new possibility. It turned out, that a spin-polarized current can transfer enough angular momentum to a magnetic system to destabilize the equilibrium orientation of the magnetization, and under certain conditions it can lead to the steady-state oscillations. This discovery has an unique feature, namely it allows to convert the energy of the dc current directly to the energy of the microwave oscillations. The phenomenon was called the spin-transfer torque (STT) effect and nowadays it is one of the most popular trends in nanomagnetism [14, 15, 16].

Initially the STT effect was intensively investigated in multilayered structures [17, 18, 19, 20, 21], where an electrical current becomes spin-polarized after passing through a thick ("fixed") magnetized magnetic layer. The electrons with spins parallel to the magnetization direction of the polarizer get transmitted and the electrons with antiparallel spins get partially reflected. After that, the output spin-polarized current is injected in a thinner ("free") magnetic layer to excite the magnetization dynamics via the STT effect.

However, recently an another possibility was demonstrated. This new method is based on pure spin currents. Their utilization not only reduces the adverse heating effects but also eliminates the need for an upper electrode, and therefore one can use magneto-optical techniques to study the spin-torque induced dynamics. Up to now in the most experiments pure spin currents have been

generated by means of the spin-Hall effect (SHE) in materials with strong spin-orbit interaction. It has been shown that pure spin currents, created in such a way, can excite ferromagnetic resonance (FMR) [23], switch the magnetization [24], control the magnetic damping [25, 26, 27, 28] and excite coherent magnetization oscillations [29, 30, 31]. Alternative way to create pure spin currents is based on the nonlocal spin injection (NLSI), which has been intensively studied in the last several years. So far it was shown to enable magnetization switching [32, 33] and to influence the magnetic damping [34, 35]. But only very recently the first spin-torque nano-oscillators based on the NLSI mechanism were demonstrated [36]. Therefore up to now little is known about their characteristics.

This thesis is devoted to a detailed study of the NLSI-based oscillators. The outline of the work is as follows. Firstly, we introduce basic theory (Chapter 2) and discuss experimental methods (Chapter 3). Then we compare the Joule heating effects in SHE and NLSI devices (Chapter 4) and show that in the latter case they are minimized. Next in Chapter 5 we study the spectral properties of the devices and prove that they exhibit a highly coherent dynamics with the spectral linewidth of a few megahertz at room temperature. Finally, in Chapter 6 we demonstrate efficient excitation and directional propagation of spin waves generated by pure spin currents.

Chapter 2

Basic Theory

2.1 Equations of magnetization dynamics

To describe the dynamical processes in magnetically ordered substances one can use the continuum approach [5, 6]. Applying it, we introduce the magnetization vector,

$$\mathbf{M}(t, \mathbf{r}) = \frac{\sum_{\Delta V} \mathbf{m}}{\Delta V}$$

which is defined as the magnetic moment per unit volume. Generally, these magnetic moments $\mathbf{m}$ comprise contributions from both the spin and the orbital motion of the electrons. The magnetization reaches its maximum value when all magnetic moments are aligned in the same direction. In this case the absolute value of $\mathbf{M}$ is called the saturation magnetization M_0.

The dynamics of the magnetization $\mathbf{M}(t, \mathbf{r})$ in an external field $\mathbf{H}_0$ is described by the Landau-Lifshitz-Gilbert (LLG) equation [37]

$$\frac{\partial \mathbf{M}}{\partial t} = -\gamma[\mathbf{M} \times \mathbf{H}_0] + \mathbf{T}_G. \tag{2.1}$$

The first term in the right-hand side leads to the precession motion of the magnetization (Figure 2.1a) about the direction of $\mathbf{H}_0$, where $\gamma \approx 2.8$MHz/Oe is the gyromagnetic ratio. The second term is the damping torque $\mathbf{T}_G$. It accounts for energy losses, which are inevitable in real-world systems. There exist several mathematical expressions for the torque $\mathbf{T}_G$ [5]. For example, the Landau-Lifshitz form

$$\mathbf{T}_G = \frac{\gamma\alpha}{M_0}[\mathbf{M} \times [\mathbf{H}_0 \times \mathbf{M}]], \tag{2.2}$$

where α is the Gilbert damping constant. As shown in Figure 2.1b, $\mathbf{T}_G$ is directed towards the precession axis, and, as a result, the oscillation amplitude gradually decreases with time.

The LLG equation, written in the form (2.1), is applicable for the description of spatially uniform excitations in an infinite magnetic media without anisotropies. In order to understand non-uniform magnetization dynamics in ferromagnetic samples with finite dimensions one has to take into account interactions between the magnetic moments. It can be done by introducing an

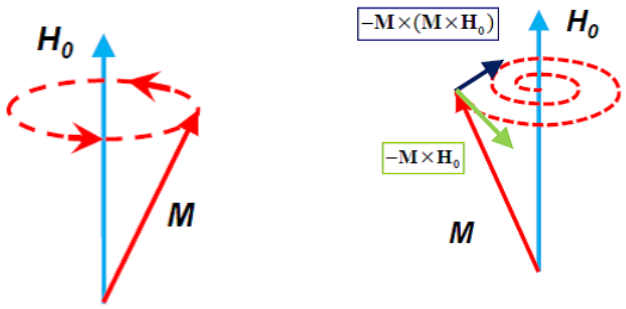

(a) (b)

Figure 2.1: (a) Precession motion of the magnetization vector M in the magnetic field $\mathbf{H}_0$. (b) Attenuation of the precession amplitude due to action of the damping torque. Used by permission from [38].

effective magnetic field $\mathbf{H}_{eff}$, which should be plugged in (2.1) instead of $\mathbf{H}_0$. In situations relevant for this thesis $\mathbf{H}_{eff}$ can be written as a sum of three terms

$$\mathbf{H}_{eff} = \mathbf{H}_0 + \mathbf{H}_{ex} + \mathbf{H}_{dem}.$$

The second field $\mathbf{H}_{ex}$ results from the short-range exchange interaction, which strength is characterized by the stiffness A. This field is significant for spin waves with wavelengths λ of the order of the exchange length $l_{ex} = \sqrt{\frac{A}{2\pi M_0}}$ [39]. For example, in $Ni_{80}Fe_{20}$ (Permalloy, further it will be referred as Py) $l_{ex} = 6$ nm [40].

The third field $\mathbf{H}_{dem}$ is induced by the long-range magnetic dipole-dipole interaction. Magnetic moments can be represented as pairs of magnetic charges in analogy to electrostatics (Figure 2.2a). They compensate each other only inside a magnetic sample, and as a result uncompensated charges emerge on the surface. These charges produce the demagnetizing field $\mathbf{H}_{dem}$ (Figure 2.2b), which is directed oppositely to the external field $\mathbf{H}_0$.

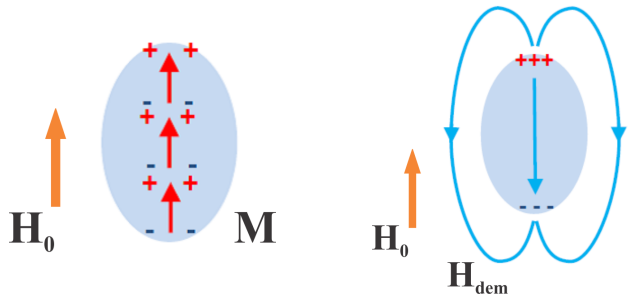

(a) (b)

Figure 2.2: (a) Elliptical shape ferromagnetic sample in the magnetic field $\mathbf{H}_0$. Magnetic moments are shown by red arrows. (b) Uncompensated surface charges give rise to the demagnetizing field $\mathbf{H}_{dem}$. Used by permission from [38].

Analytically the demagnetization field $\mathbf{H}_{dem}$ can be calculated only for relatively simple geometries [41], and in general it is a nontrivial mathematical task [42] even for the simplest case of uniform magnetization. Therefore various micromagnetics simulations packages are usually used for the calculations of spatial distributions of $\mathbf{H}_{dem}$. In Chapter 6 we will show how the demagnetizing effects can be utilized to achieve good spectral matching between the NLSI-based nano-oscillator and the magnonic nano-waveguide.

2.2 Spin-transfer torque effect

The spin-transfer torque (STT) effect discovered in 1996 by Slonczewski [12] and Berger [13] opened a new possibility for generation of microwave oscillations. They demonstrated that a spin-polarized current can transfer enough angular momentum to a magnetic system to destabilize the initial equilibrium orientation of the magnetization. In other words, the current exerts an additional torque $\mathbf{T}_S$ on $\mathbf{M}$. Under certain conditions the steady-state precession of the magnetization can be excited. This phenomena was named the spin transfer torque (STT) effect, and nano-sized microwave devices, based on it, are called spin torque nano-oscillators (STNO) [16, 22]. Common STNO geometry is shown in Figure 2.3a. It consists of two ferromagnetic layers separated by a non-magnetic film. The first magnetic layer is a relatively thick ("fixed") film, which serves as a polarizer. After passing it, an electrical current becomes spin-polarized (Figure 2.3b) and can causes the magnetization oscillations in the second thin ("free") magnetic film.

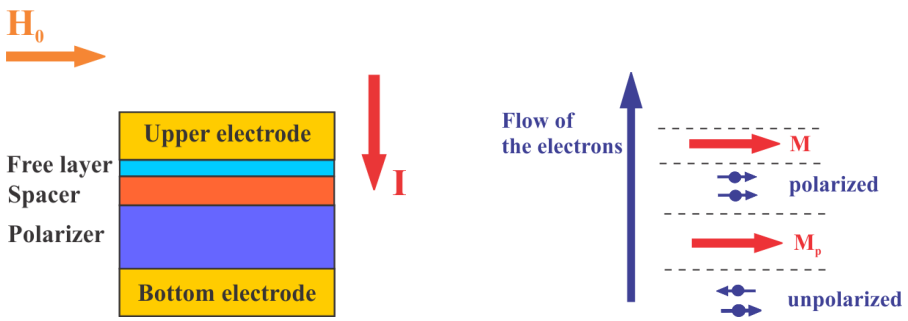

Figure 2.3: (a) Sketch of a regular spin-torque nano-oscillator. (b) Flow of the electrons becomes spin-polarized after passing though the polarizer. If the current density is sufficiently high, this flow can transfer enough angular momentum to destabilize the equilibrium orientation of the magnetization M in the top magnetic layer.

It was shown [43, 15] that the magnetization dynamics, excited by means of the spin-polarized current I, can be described by the LLG equation (2.1) with an additional torque

$$\frac{\partial \mathbf{M}}{\partial t} = -\gamma[\mathbf{M} \times \mathbf{H}_0] + \mathbf{T}_G + \mathbf{T}_S, \tag{2.3}$$

which can be written as

$$\mathbf{T}_S = \frac{\sigma_0 I}{M_0}[\mathbf{M} \times [\mathbf{M} \times \mathbf{e}_p]]. \tag{2.4}$$

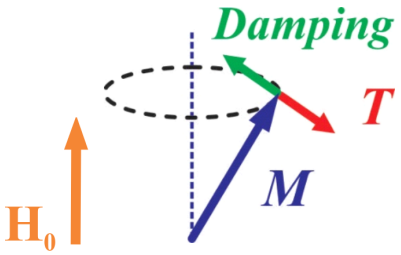

Figure 2.4: Under certain conditions, the direction of the spin-transfer torque can be antiparallel to that of the dynamic damping torque. It can lead either to the switching or to the stable precession of the magnetization M. Used by permission from [38].

Here $\mathbf{e}_p$ is the unit vector directed along the fixed-layer magnetization and coefficient σ is given by

$$\sigma_0 = \frac{\epsilon g \mu_B}{2eM_0LS},$$

where g is the Lande factor, μ_B is the Bohr magneton, L is the thickness of the "free" magnetic layer, S is the area of the current injection and parameter ϵ defines the degree of spin polarization ($|\epsilon| < 1$).

As follows from (2.4), the direction of the spin-transfer torque depends on relative orientation of $\mathbf{e}_p$ with $\mathbf{M}$ and the current sign. When $\mathbf{T}_S$ is parallel with the damping torque $\mathbf{T}_G$, the STT just enhances the natural magnetic damping, and it can be described as increase of the Gilbert damping constant α. The second case $\mathbf{T}_S \| -\mathbf{T}_G$ (Figure 2.4) is more sophisticated. For example, it can lead ether to the magnetization switching or to the stable magnetization precession. Both situations are interesting from an application point of view. For example, reversal of the magnetization direction can be utilized to flip the active elements in the second generation of magnetic random-access memory, called STT-MRAM. At this moment it is under active industrial development [44]. In its turn, the steady-state magnetization precessions excited by the spin-transfer torque effect open a new method for generation of microwave signals. An analytic theory of the current-induced magnetization dynamics is discussed in the next section.

2.3 Magnetization auto-oscillations

In addition to well known force and parametric oscillations, there also exist so-called auto-oscillations, which are common for systems with a positive feedback between a oscillator and an external energy source [45]. This coupling results in an effective "negative damping", which has a form, similar to the term, which describes the natural damping, but with an opposite (negative) sign. Auto-oscillations phenomena are widely spread in nature (e.g. heartbeat) and technology (e.g. Van der Pol oscillator). But regardless of their physical realization, these systems can be described by the general equation [46]

$$\frac{dc}{dt} + i\omega(|c|^2)c + \Gamma_+(|c|^2)c - \Gamma_-(|c|^2)c = 0, \tag{2.5}$$

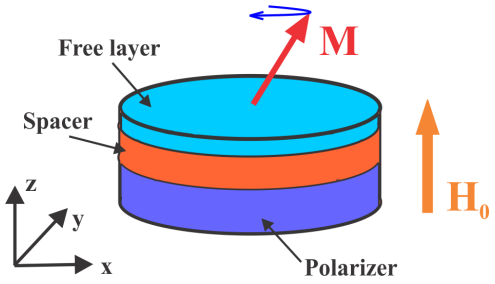

Figure 2.5: Normally magnetized nanopillar. The magnetization M precesses around the z axis.

where $c(t)$ is the complex amplitude, which determines both the power $p = |c|^2$ and the phase $\phi = arg(c)$ of the oscillations. In (2.5), $\omega(p)$ is the system eigenfrequency, positive damping $\Gamma_+(p)$ is associated with the natural energy dissipation and negative damping $\Gamma_-(p)$ describes the action of the external force, which compensates the losses. Limits of validity of the model (2.5) are discussed in [46].

Now we will show how (2.5) can be used to describe the current-induced magnetization oscillations. An important feature of the Landau-Lifshitz-Gilbert-Slonczewski equation (2.3) is the conservation of the magnetization length. In other words, two components of the vector $\mathbf{M} = (M_x, M_y, M_z)$ are enough to describe the system's dynamics. For example, for a normally magnetized nanopillar, shown in Figure 2.5, we can introduce a new complex variable as

$$c = \frac{M_x - iM_y}{\sqrt{2M_0(M_0 + M_z)}}. \tag{2.6}$$

This dimensionless amplitude c provides the simplest description of the magnetization dynamics, and in this case it is connected to the precession angle $\psi = arccos(1 - 2|c|^2)$. Therefore only the values $|c| < 1$ have a physical meaning. In general the spin-wave amplitude $c = c(M_x, M_y)$ is a complex function of the magnetization components.

By using the new variable c, one can rewrite the Landau-Lifshitz-Gilbert-Slonczewski equation (2.3) in the general form (2.5). In the case of the nanopillar (Figure 2.5) it can be done explicitly [46]. For other geometries of STNOs with abritrary direction of the external magnetic field the same reduction is also possible, but only approximately [47, 48]. We are not going to discuss the entire procedure here, all details can be found in [46].

The first precession torque $-\gamma[\mathbf{M} \times \mathbf{H}_{eff}]$ in the right-hand side of (2.3) can be rewritten as $i\omega(|c|^2)c$ where $\omega(|c|^2)$ is the nonlinear precession frequency

$$\omega(|c|^2) \approx \omega_0 + N|c|^2. \tag{2.7}$$

Here N is the coefficient of the nonlinear frequency shift, which sign depends on the direction of the external magnetic field H_0. For normally magnetized systems $N > 0$ and thus the operation frequency increases with increasing oscillations intensity. For the in-plane geometry $N < 0$, so the frequency $\omega(p)$ decreases with increasing p. The Gilbert damping torque $\mathbf{T}_G$ becomes $\Gamma_+(|c|^2)c$ where

$$\Gamma_+(|c|^2) \approx \Gamma_G(1 + Q|c|^2) \tag{2.8}$$

The damping function $\Gamma_+(|c|^2)$ is always positive and therefore leads to the decrease of the spin-wave amplitude c with time. In a similar way the STT term $\mathbf{T}_S$ can be rewritten as $-\Gamma_-(|c|^2)c$ where

$$\Gamma_-(|c|^2) = \sigma I(1 - |c|^2). \tag{2.9}$$

$\Gamma_-(|c|^2)$ is positive for $I > 0$ thus the spin transfer torque exerts effective negative damping on the magnetization in the "free" magnetic layer. All the formulas (2.7 - 2.9) are written in the limit of small powers p, and the explicit expressions for the expansion coefficients $\omega_0, N, \Gamma_G, Q, \sigma$ can be found in the appendix to [46].

In order to analyze possible solutions of (2.5), it is convenient to rewrite (2.5) in terms of the power $p = |c|^2$ and the phase $\phi = arg(c)$. Then the general model (2.5) becomes a system of two equations

$$\frac{dp}{dt} = -2[\Gamma_+(p) - \Gamma_-(p)]p \tag{2.10}$$

$$\frac{d\phi}{dt} = -\omega(p).$$

The first equation (2.10) has two stationary solutions. The first one $p_0 = 0$ is uninteresting because it corresponds to the absence of any oscillations. Applying linear stability analysis, one can find that the solution is stable provided $\Gamma_+(0) > \Gamma_-(0)$. Therefore the condition $\Gamma_+(0) = \Gamma_-(0)$ defines the critical current I_c at which the negative damping completely compensates the natural energy dissipation. As a result the initial state $p_0 = 0$ loses its stability and the system makes a transition to the auto-oscillation regime. The second possible solution is $p = p_0$, where p_0 is determined from the condition $\Gamma_+(p_0) = \Gamma_-(p_0)$. This equality has a clear physical meaning: in the auto-oscillation regime ($p = p_0$), the energy losses due to the intrinsic damping $\Gamma_+(p_0)$ should be exactly compensated by the effective negative damping $\Gamma_-(p_0)$ created by the spin-transfer torque effect.

The equation (2.5) describes free or autonomous auto-oscillators. However, usually one should take into account various noise sources, for example, thermal fluctuations, which play a significant role in the case of nano-oscillators. As a result their characteristics like the generated power or the spectral linewidth depend on the temperature. In the presence of noise the general equation can be rewritten as

$$\frac{dc}{dt} + i\omega(|c|^2)c + \Gamma_+(|c|^2)c - \Gamma_-(|c|^2)c = f_n(t), \tag{2.11}$$

where an external force $f_n(t)$ describes the action of thermal fluctuations.

The detailed analysis of (2.11) can be found in [46]. Here we only briefly describe results which we will use later to interpret experimental data. At first, it can be shown that the inverse mean power depends on the driving current as

$$\frac{1}{\bar{p}} \sim (I_c - I)$$

in the below-threshold region (before the magnetization starts to auto-oscillate). By using this fact, one can precisely determine the critical current I_c. The measured values of $1/\bar{p}$ should be plotted versus I and be interpolated by a linear function. Its intersection with the horizontal

axis marks the critical current I_c. In the next chapters we will use this method, but instead of linear fitting we will utilize polynomial interpolation. This discrepancy can be explained by the fact that (2.11) was derived in a macrospin approximation, while we will study the nonuniform magnetization dynamics.

The second important result derived in [46] is a form of the power spectrum $S(\omega)$. It can be shown that $S(\omega)$ is a simple Lorentzian function

$$S(\omega) \sim \frac{\Delta\omega}{(\omega - \omega_0)^2 + \Delta\omega^2},$$

where ω_0 is the central auto-oscillation frequency and $\Delta\omega$ is the spectral linewidth. Thus by fitting the detected peaks with Lorentzian functions, we can precisely determine both ω_0 and $\Delta\omega$.

2.4 Pure spin currents

Up to now in many experiments the magnetization dynamics driven by the spin-transfer torque effect have been studied in systems similar to that shown in Figure 2.3a. An electrical current after passing through the fixed layer becomes spin-polarized due to spin-dependent scattering. Then the current is injected into the "free" magnetic layer, where it excites microwave oscillations due to the STT effect. Thank to the giant magnetoresistance (GMR) effect the magnetization motion is converted into differential resistance $\frac{dV}{dI}$ variations, which can be directly measured (Figure 2.6). The first observations of the magnetization dynamics driven by the spin-transfer torque were made by using this method [17, 19, 18, 20].

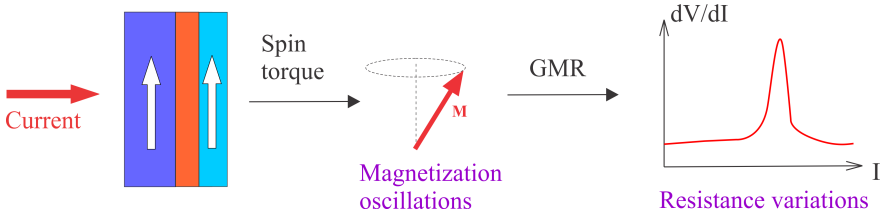

Figure 2.6: Scheme of early experiments studied the STT effect.

Another possibility to excite the magnetization oscillations is to use so-called pure spin currents. Unlike conventional currents, they are not accompanied by the charge flow (Figure 2.7) and therefore have a few advantages which make them promising for technical applications. At first, the electrical current doesn't flow through the magnetic layer. Therefore less Joule heating is expected and potentially one can use low-loss dielectric magnetic materials such as yttrium iron garnet (YIG). Secondly, the upper electrode isn't necessary and that gives us the possibility to create devices with very flexible layouts. Finally one can use magneto-optical techniques (like Brillouin light scattering spectroscopy) to study the magnetization dynamics driven by the spin-transfer torque effect.

One of the ways to create pure spin currents is based on the Spin-Hall effect (SHE) [49, 50] in materials with strong spin-orbit interaction, such as platinum (Pt). Due to the spin-dependent

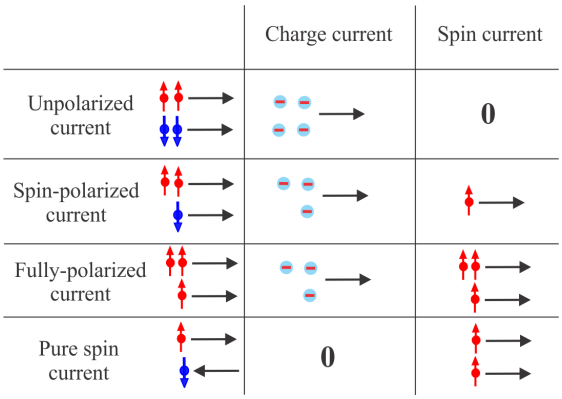

Figure 2.7: Various types of electrical currents.

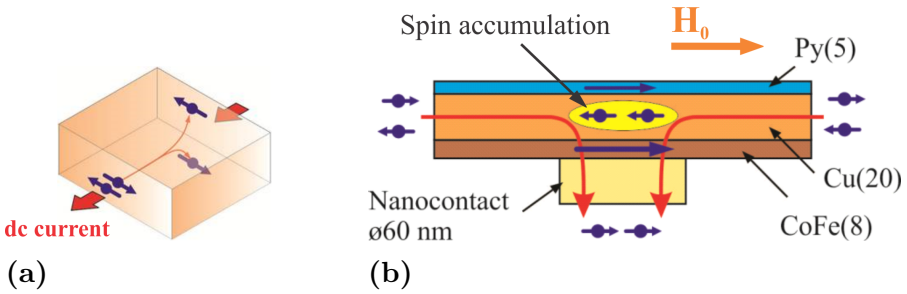

Figure 2.8: (a) Spin-Hall effect. The electrical current creates a spin accumulation at the lateral boundaries of the Pt film. (b) Sketch of the NLSI-oscillator operation principle. Red arrows represent the flow of the electrons. Small purple arrows show the magnetic moments carried by the electrons. Used by permission from [38].

scattering on impurities and defects, when a direct current flows in the plane of the Pt film, electrons carrying opposite magnetic moments are deflected toward the opposite surfaces (Figure 2.8a). If we place a magnetic layer on top of the film, the spin current exerts the spin-transfer torque on its magnetization. Extensive discussions of this phenomena can be found in [51, 52, 53]. After the first demonstration of excitation of coherent auto-oscillations by pure spin currents generated by the spin-Hall effect [29], intense experimental and theoretical studies were induced [54, 31, 55, 56]. To date the SHE-based oscillators have been implemented in the form of nano-gaps [29], nano-constrictions [30] and nano-wires [31].

Alternative way to create pure spin currents is based on utilization of the nonlocal spin-injection (NLSI) mechanism. There exist several possible geometries [32, 34, 35] but in this thesis we will discuss only a system depicted in Figure 2.8b. It is a three-layer Py(5)Cu(20)CoFe(8) structure (in parenthesises thicknesses in nanometers are specified) with a circular 60-nm diameter Au nanocontact in the center. An in-plane magnetic field $\mathbf{H}_0$ is applied, which saturates the magnetizations of both the Py and the CoFe layers. Therefore the electrons with magnetic moments aligned in the opposite direction scatter at this interface between the Cu and CoFe layers and create a non-equilibrium spin accumulation above the nanocontact. Then these electrons diffuse into the Py layer and exert the spin-trasfer torque on its magnetization. The resulting STT acts in the

opposite direction to the Gilbert torque $\mathbf{T}_G$, and when the damping is completely compensated, the magnetization of the Py film starts to auto-oscillate. This mechanism is called the nonlocal spin-injection and the first spin-torque nano-oscillator based on it was demonstrated very recently [36].

Chapter 3

Methods

3.1 Micro-focus Brillouin light scattering spectroscopy

There are several experimental methods for studying magnetization dynamics in magnetic samples [1, 3]. For example, antenna-based microwave spectroscopy or magneto-optical techniques based on Kerr and Faraday effects. However, probably the most powerful tool is micro-focus Brillouin light scattering (BLS) spectroscopy [57], which combines high sensitivity (it allows to analyze the magnetization dynamics excited due to thermal fluctuations) with sufficient frequency and spatial resolutions. The BLS setup is shown in Figure 3.1 and described in detail in [57, 58].

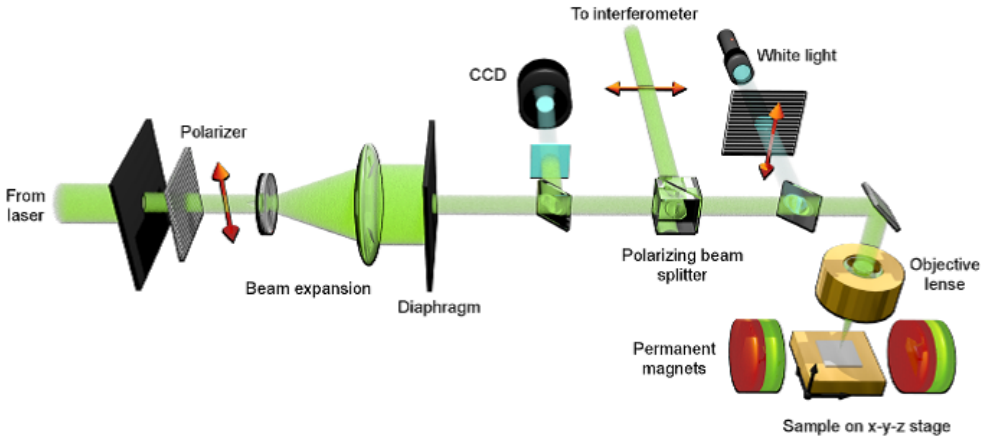

Figure 3.1: Scheme of the micro-focus BLS setup. Figure used by courtesy of Henning Ulrichs (p. 33 in [58]).

Brillouin scattering itself is an interaction between an incident electromagnetic wave and collective excitations in a studied system. From a quantum point of view, it can be describe as an

inelastic scattering of photons on quisiparticles (magnons, in our case). Two processes with equal probabilities are possible. A photon of energy $\hbar\omega_1$ absorbs a magnon of energy $\hbar\omega_M$ (Figure 3.2a) and therefore acquires additional energy due to the conservation law. Or in the reverse process (Figure 3.2b) it creates a magnon and consequently loses some amount of energy.

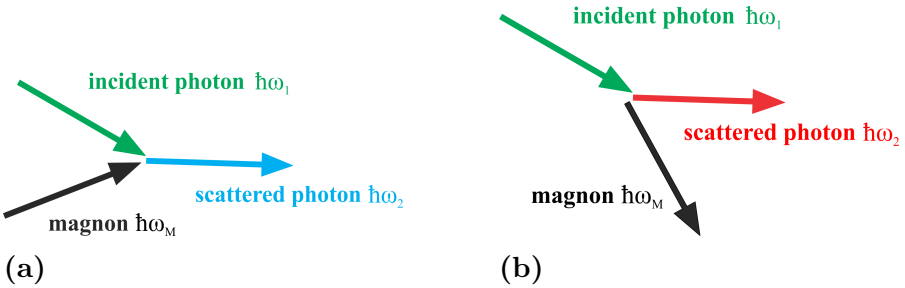

Figure 3.2: (a) Scattering with magnon absorption $\hbar\omega_2 = \hbar\omega_1 + \hbar\omega_M$. (b) Scattering with magnon creation $\hbar\omega_2 = \hbar\omega_1 - \hbar\omega_M$. Used by permission from [38].

In our experiments we used a laser with a wavelength of 532 nm and the output power less than 1 mW. By using microscope objective lens, it is possible to focus the laser beam into a diffraction-limited spot onto the surface of the magnetic sample (Figure 3.3), which is mounted on a piezoelectric stage. Permanent magnets produce a static external magnetic field $\mathbf{H}_0$. A CCD camera with additional white light is used to control the position of the stage and the probing laser spot.

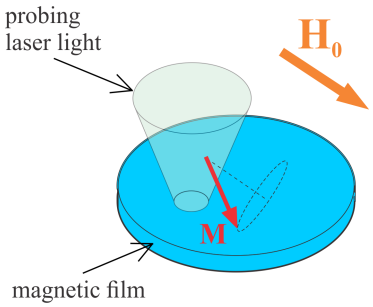

Figure 3.3: Magnetization dynamics studied by means of BLS spectroscopy.

The scattered light is collected by the same objective lens and then analyzed by means of an interferometer (we used a six-pass Fabry-Perot interferometer TFP-1 [59]). Figure 3.4 schematically shows measured spectrum. It contains a peak at the frequency of the incident light and two additional peaks at frequencies shifted by the magnon frequency ω_M, which intensities are proportional to the intensity of magnetization oscillations at the position of the probing spot [60]. It should be noted, that the output spectrum is always a convolution of the input spectrum with the instrumental function. Therefore the frequency resolution is limited down to 50 MHz. In order to measure the spectral linewidths more precisely one should use microwave spectroscopy.

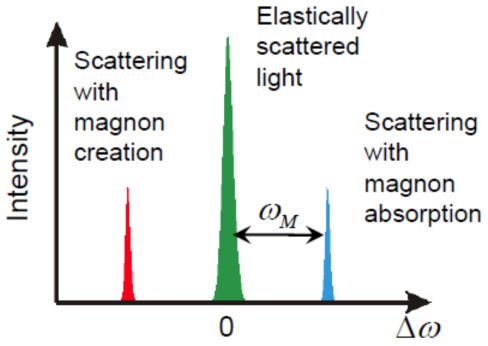

Figure 3.4: Schematic picture of a measured spectrum. Used by permission from [38].

Additionally to frequency-domain measurements, we can use the micro-focus BLS technique to perform spatial measurements. For that one should scan a sample by the probing laser beam and measure the intensity of the spectral peaks at every spatial point (Figure 3.5a). As a result, a two-dimensional color map is recorded like shown in Figure 3.5b. Spatial resolution is determined by the size of the laser spot, which in our experiments is focused down to the diffraction limit of 250 nm.

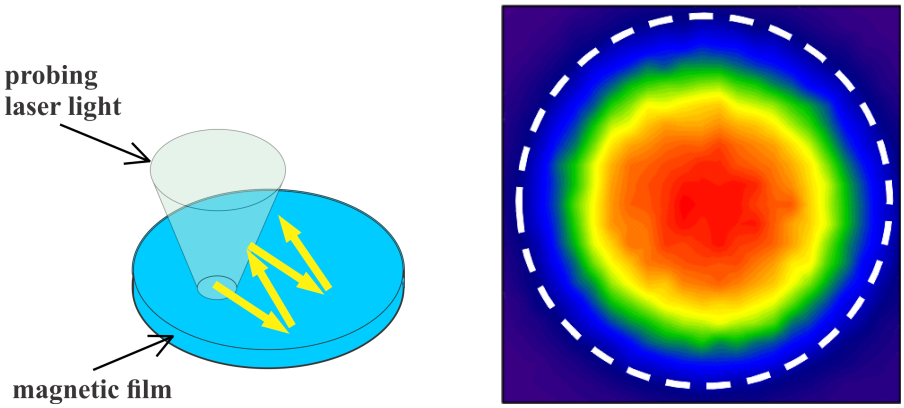

(a) (b)

Figure 3.5: (a) Spatial BLS measurements. (b) Spatial map recorded at the frequency of the center mode. The measured intensity is proportional to the local intensity of magnetization oscillations. Used by permission from [38].

3.2 Micromagnetic simulations

Nowadays computer simulations play a great role in physics. They are used as a powerful auxiliary tool which helps to elucidate complicated dynamics of a studied system and to interpret experimental data. In micromagnetics there are many different simulation packages, among which OOMMF [61] is the most popular. But recently a new kind of software MuMax3 [62] was presented which is based on utilization of graphics card processing instead of conventional CPU's. That

significantly increases computational speed, and therefore makes this newcomer very attractive for researchers. In this thesis we will use MuMax3 for two purposes: calculation of the demagnetization field $\mathbf{H}_{dem}$ and calculation of the dispersion relation for spin waves propagating in the magnonic nano-waveguide.

Mumax3 uses the finite difference method to solve the LLG equation (2.1) numerically. It means that after one defines a number of simulation cells $N = N_x \cdot N_y \cdot N_z$, the package represents the sample geometry by rectangular mesh with appropriate size of cells. Additionally values of necessary material parameters like the saturation magnetization M_0, the exchange constant A and the Gilbert damping parameter α should be specified.

Next, the ground state of the system is computed. For that a static external field $\mathbf{H}_0$ is applied and the LLG equation (2.1) is integrated for 10 ns. From the calculated data one can extract the internal field $\mathbf{H}_{int} = \mathbf{H}_0 + \mathbf{H}_{dem}$. The same procedure will be used in the first section of Chapter 6.

Then, depending on the task, one should determine an external excitation. We will use an inhomogeneous magnetic field, which form described in the third section of Chapter 6. After that, time integration of the LLG equation is performed for the total time t and the vector field $\mathbf{M}$ is saved at equidistant time steps Δt.

For post-processing we use a method suggested by McMicheal and Stiles [63]. At first, we perform Fourier transform of the time evolution $m_i(t)$ of each cell. As a result we get so-called local spectra $m_i(f) = \mathcal{F}[m_i(t)]$. Then by using the formula

$$m(f) = \sum_{i=1}^{N} m_i(f),$$

one can calculate the integral spectrum, where spin wave modes appear as peaks (Figure 3.6).

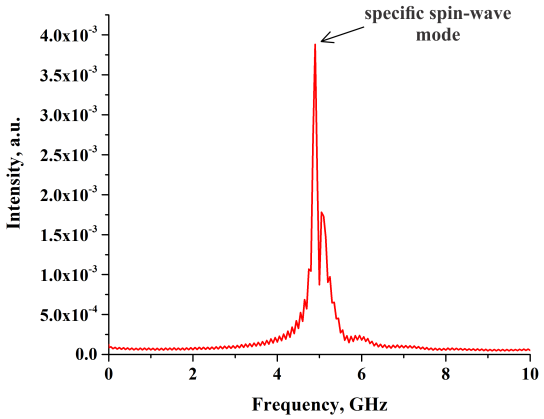

Figure 3.6: Spin-wave spectra obtained after the post-processing procedure.

Chapter 4

Joule heating in nano-oscillators

When a charge current flows through a conductor, the electrical resistance leads to a local temperature increase. This effect is called Joule heating, and in most cases it is undesirable because it accelerates degradation of a structure and adversely affects dynamics (e.g., spectral properties) of a studied system. In this chapter we discuss the Joule heating effects in both SHE- and NSLI-based oscillators.

4.1 SHE-based oscillator

We chose a nanoconstriction oscillator [30] as an example of a device based on the spin-Hall effect. The system is depicted in Figure 4.1. It is a Py(5)Pt(8) bilayer strip (in parenthesises thickhesses in nanometers are specified) of width 4 μm in the x-direction. The width of the bow tie-shaped constriction is 150 nm, the radius of curvature is 50 nm and an opening angle is about 22°.

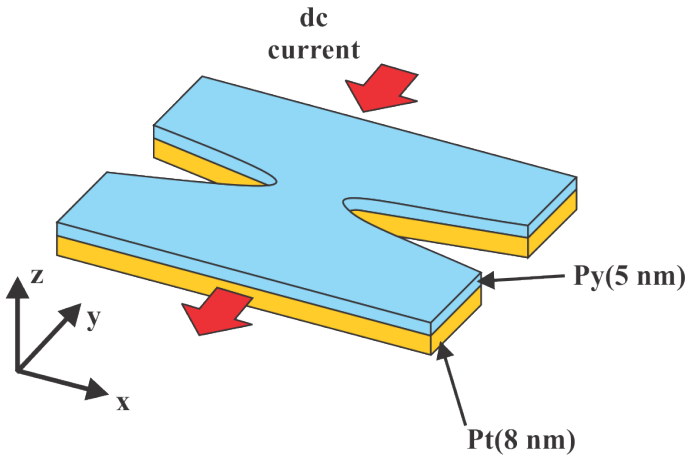

Figure 4.1: Sketch of the SHE-based device.

At first we calculated the distribution of the current density $\mathbf{j}_c$ in the entire structure. For that we used COMSOL Multiphysics [64]. It is a simulation software, which can solve Maxwell's

equations by utilizing the finite element method. For the resistivities we used the following values: $\rho_{Pt} = 11.2 \pm 0.6\mu\Omega \cdot cm$ and $\rho_{Py} = 32.6 \pm 0.6\mu\Omega \cdot cm$ [30]. For other material parameters we assumed bulk values, which can be found in the appendix.

Figure 4.2 shows the calculated spatial distribution of $\mathbf{j}_c$ in the plane of the Pt layer. As seen from the data, the constriction leads to a local increase of the current density and this region defines the active device area [30].

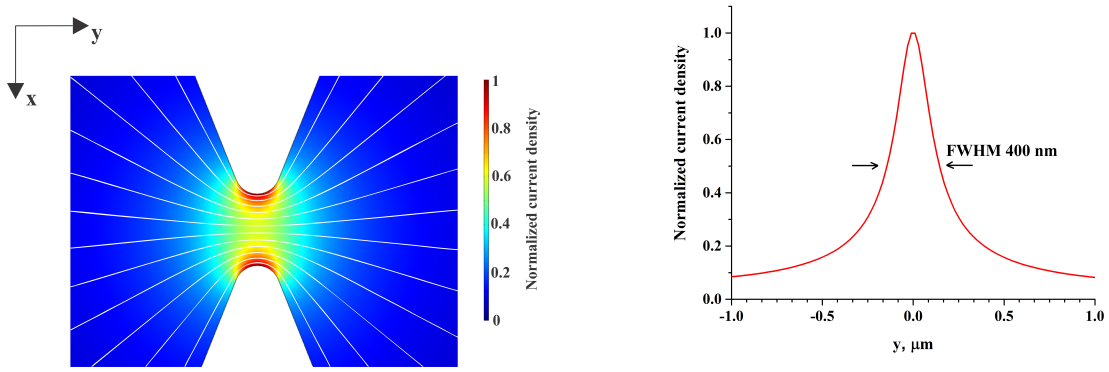

(a) (b)

Figure 4.2: (a) Normalized color-coded map of the current density in the plane of the Pt layer. White curves are streamlines. (b) Profile of the normalized current density along the y-axis. The data were calculated at $I = 5$ mA.

Figure 4.3 shows the current density along a vertical section. We can estimate that approximately 80% of the current is drained through the Pt layer while the rest 20% flows through the magnetic Py layer.

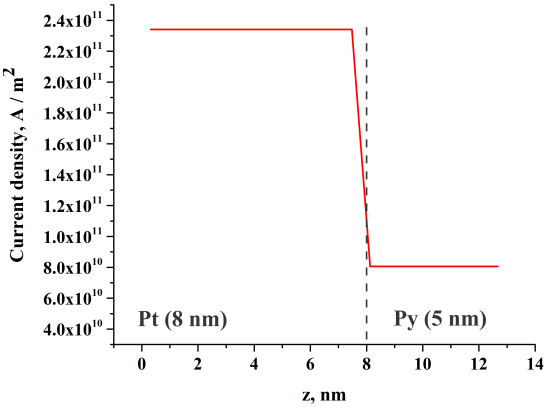

Figure 4.3: Current density distribution along the z-axis in the center of the system. The data were calculated at $I = 5$ mA.

To estimate the magnitude of Joule heating effects in the SHE-based oscillators we extended our model by the heat flow equations. The room temperature was set to $T_0 = 293.15K$. The calculated temperature increase $\Delta T = T - T_0$ is shown in Figure 4.4. As expected from Figure 4.2, ΔT is highest in the nanoconstriction region because of the local increase of the current density.

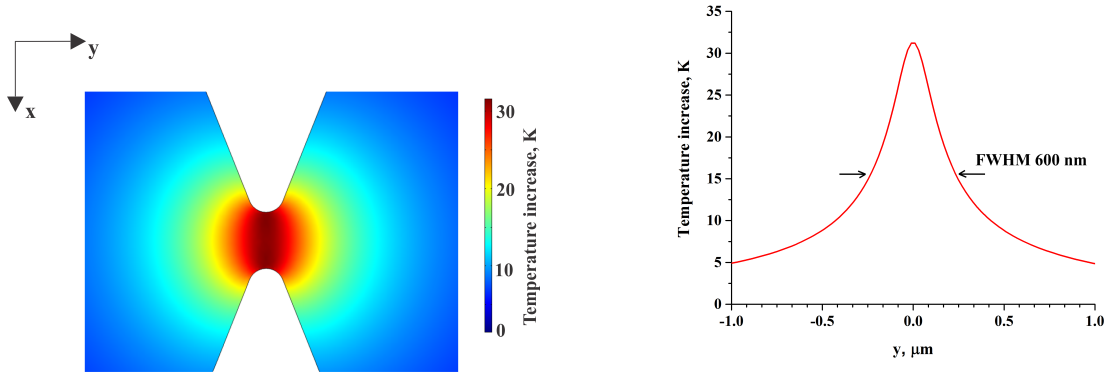

(a) (b)

Figure 4.4: (a) Color-coded map of the temperature increase ΔT in the plane of the Pt layer. (b) ΔT as a function of the y-coordinate. The data were calculated at $I = 5$ mA.

To find the dependence of the Joule heating magnitude on the driving current we plotted $\Delta T_{max} = T_{max} - T_0$ (where T_{max} is a temperature in the center of the system) as a function of I (Figure 4.5). The current range corresponds to that used in [30].

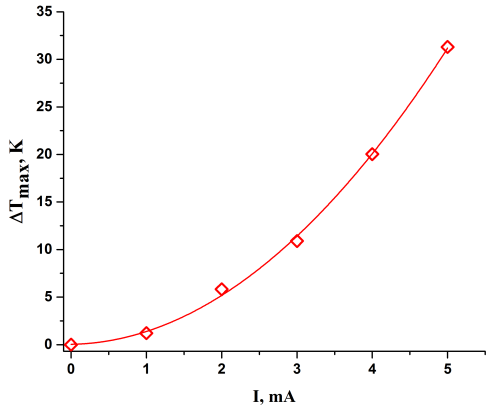

Figure 4.5: Maximum temperature increase vs. current. Open diamonds are calculated values, curve is the result of parabolic fit.

4.2 NLSI-based oscillator

In this section we analyze the NLSI-based oscillator [36]. The system is depicted in Figure 4.6. It consists of a three-layer CoFe(8)Cu(20)Py(5) disk with a diameter of 3 μm and with attached 2 μm wide strip, which connects the device to the external contact. A circular 60-nm diameter Au nanocontact is placed in the center of the structure.

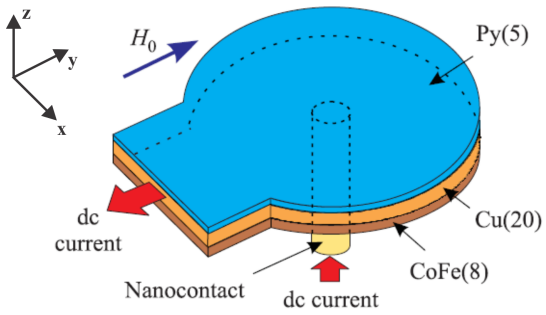

Figure 4.6: Sketch of the NLSI-based device. Used by permission from [36].

As in the case of the SHE oscillator at first we calculated the spatial distribution of $\mathbf{j}_c$ by means of COMSOL Multiphysics. For the resistivities we used values provided by S. Urazhdin: $\rho_{Py} = 40\ \mu\Omega \cdot cm$, $\rho_{Cu} = 6.25\ \mu\Omega \cdot cm$ and $\rho_{CoFe} = 25\ \mu\Omega \cdot cm$. For other material parameters we assumed bulk values, which can be found in the appendix.

Figure 4.7 shows the computed spatial distribution of the current density. As shown in Figure 4.7a, the streamlines are almost radially symmetric in the vicinity of the nanocontact and therefore an Oersted field produced by the current is negligible in this region.

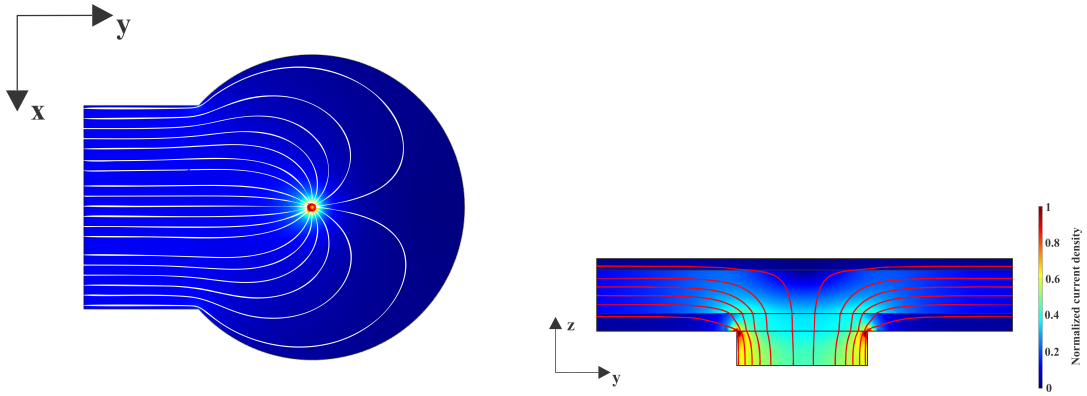

(a) **(b)**

Figure 4.7: Distribution of the current density in the plane of the Cu layer (a) and in the vertical cross-section (b). White and red curves are streamlines. The data were calculated at $I = 12$ mA.

To estimate the portion of the driving current, which flows thought the magnetic layer, we

plotted the current density along a vertical section away from the contact area (Figure 4.8). It demonstrates that about 88% of the current is concentrated in the Cu layer, nearly 9% is drained through the CoFe layer and only 3% flows across the Py layer.

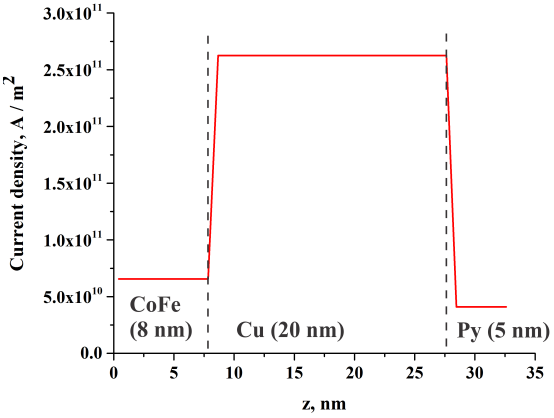

Figure 4.8: Current density distribution along the z-axis away from the nanocontact area. The data were calculated at $I = 12$ mA.

Next we investigated the Joule heating effects in the NLSI-based oscillators. Again we added the standard heat flow equations to our model and set the room temperature to $T_0 = 293.15K$. The calculated temperature distribution is shown in Figure 4.9. As it is expected from the current density simulation (Figure 4.7a), the region of the highest temperature increase ΔT is an area around the nanocontact.

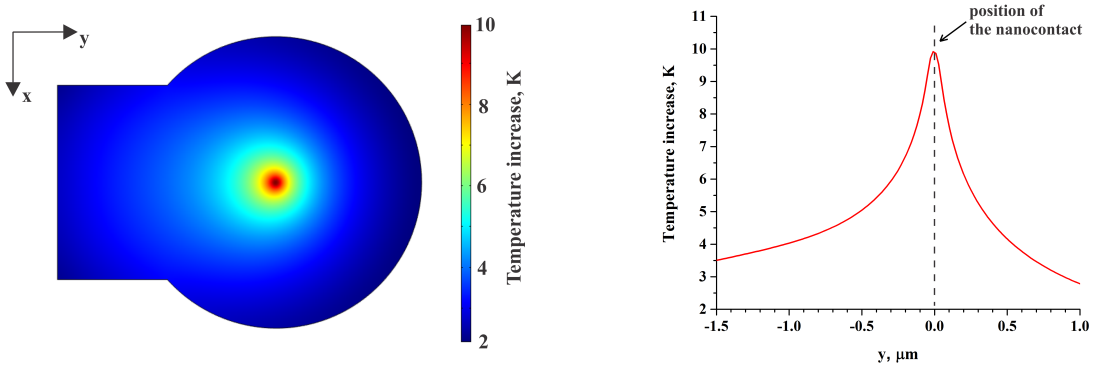

(a) **(b)**

Figure 4.9: (a) Color-coded map of the temperature increase ΔT in the plane of the Cu layer. (b) ΔT as a function of the y-coordinate. The data were calculated at $I = 12$ mA.

Figure 4.10 shows the dependence of the maximum temperature increase $\Delta T_{max} = T_{max} - T_0$

(where T_{max} is a temperature in the center of the system) on the driving current I. The current range corresponds to that used in [36].

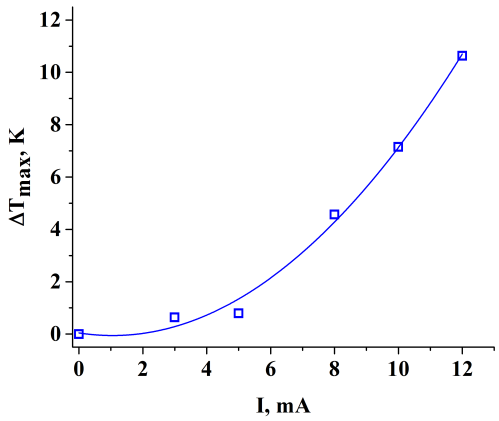

Figure 4.10: Maximum temperature increase vs. current. Open squares are calculated values, curve is the result of parabolic fit.

4.3 Conclusions

From these calculations we can conclude that the NSLI-based devices have several advantages over the SHE-based. At first, materials with strong spin-orbit coupling such as Pt have relatively high resistivity. As a result, in the SHE oscillators significant portion of the driving current flows through the magnetic layer (about 20%, Figure 4.3). In the NLSI oscillators copper is used instead of platinum which revistivity ρ_{Cu} is smaller by a factor of five. Therefore the driving current flows mostly through the low-resistivity layer, and the Py film contribution is almost negligible (less than 3%, Figure 4.8). Thus, the Joule heating effects are minimized in these structures. In order to prove it we plotted the maximum temperature increase ΔT_{max} for the SHE- and the NLSI-based oscillators in one graph. Figure 4.11 demonstrates that, for example, at $I = 2I_c$ (the definition of the critical current is given in Chapter 2) the temperature increase ΔT_{max} for the SHE oscillators is large than 50 K, while for the NLSI oscillators $\Delta T_{max} < 6K$.

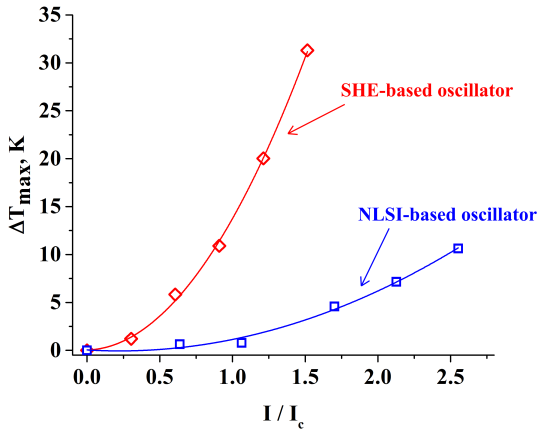

Figure 4.11: Comparison of the Joule heating magnitudes.

Additionally, in the SHE devices materials with strong spin-orbit coupling affect the Gilbert damping constant α in the Py layer, increasing it by a factor of two [65]. The NLSI oscillators don't suffer from this detrimental effect. Finally, the current flow is almost radially symmetric in the vicinity of the nanocontact (Figure 4.7a), and that leads to a negligible Oersted field in this kind of structures. All these features demonstrate a significant potential of the nonlocal oscillators for technical applications.

Chapter 5

Spectral linewidth of nano-oscillators driven by nonlocal spin injection

For any microwave oscillator its spectral linewidth is among the most important characteristics. The recently demonstrated NLSI-based oscillators [36] were found to exhibit relatively small auto-oscillation linewidths in the range of 13 to 20 MHz. But these values are only upper estimations because the oscillators were studied only by means of micro-focus Brillouin light spectroscopy [57], which frequency resolution is limited, and therefore further research is needed. In this chapter we present a detailed study of the spectral properties of the NLSI-based devices. Additionally to the BLS technique we used electronic microwave spectroscopy, which allows us to perform high-resolution spectral analysis of auto-oscillations induced by pure spin currents.

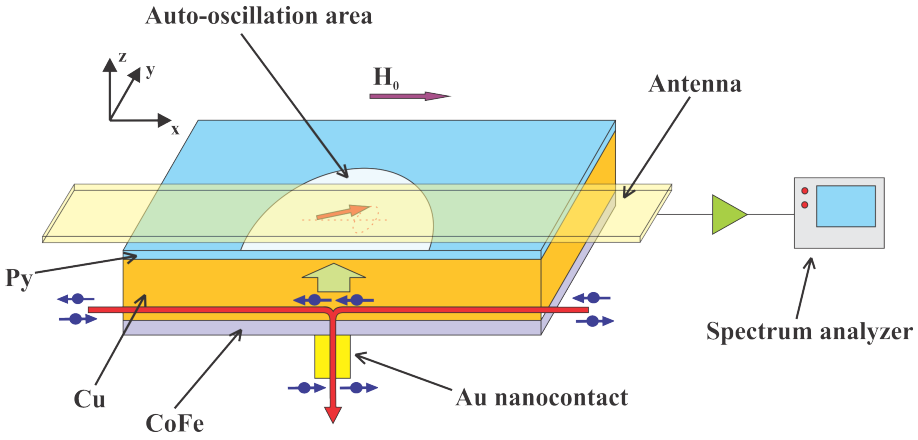

Figure 5.1: Sketch of the NLSI nano-oscillator with a built-in inductive antenna. The insulting layer SiO_2 between the Py film and the antenna is not shown.

The sketch of a studied nano-oscillator is shown in Figure 5.1. It is a three-layer structure Py(5)Cu(20)CoFe(8) with a 60 nm diameter Au nanocontact in the center. In order to use electronic spectroscopy we integrated the device with an inductive antenna. It is a 200 nm wide and 30 nm thick Au stripe which separated from the active area by a 20 nm thick insulating layer of SiO_2.

The operation of the device is described at the end of the second chapter. When the spin-transfer torque completely compensate the natural magnetic damping, the magnetization of the Py layer starts to auto-oscillate. It produces the oscillating magnetic field which induces a microwave current in the antenna. Then the signal is amplified and detected by a spectrum analyzer.

5.1 BLS measurements

At first, we studied properties of the system by means of micro-focus BLS spectroscopy. One of its advantages is high sensitivity which allows us to investigate the magnetization dynamics before the onset of high-intense auto-oscillations. A spatial map recorded with help of the BLS technique is shown in Figure 5.2. The measured intensity is proportional to the local intensity of the dynamic magnetization. Therefore from the figure we can estimate the size of the auto-oscillation area and, as in the case of previously studied NSLI oscillators [36], it exceeds 300 nm in a diameter. A slight asymmetry of the picture can be explained by a small misalignment of the structure.

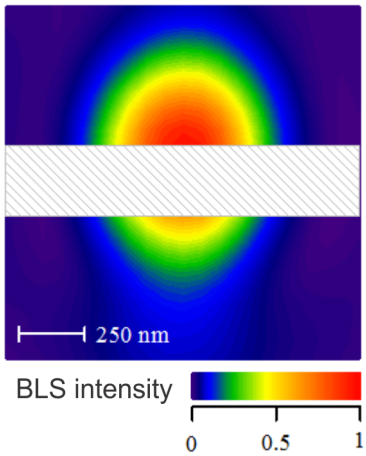

Figure 5.2: Normalized spatial map of the BLS intensity measured at $I = 7$ mA and $H_0 = 1000$ Oe. Shaded area shows the inductive antenna.

Next we placed the probing light spot near the edge of the antenna and investigated the influence of the driving current I on the magnetization oscillations in the Py layer. Figure 5.3 demonstrates BLS spectra measured for different currents. In Figure 5.3a a broad spectrum associated with thermally excited magnons is shown at $I = 0$ (black symbols). Below the onset of auto-oscillations small applied current enhances thermal fluctuations [26], therefore the magnetization oscillations becomes more intense and the corresponding spectrum narrows (Figure 5.3a, red symbols). As discussed in Chapter 2, at the critical current I_c the effective negative damping, created by the STT effect, completely compensates the natural magnetic damping, and the system makes a transition to the auto-oscillation regime. In the spectrum it is manifested by appearance of an intense peak (Figure 5.3b, note the scale change on the vertical axis).

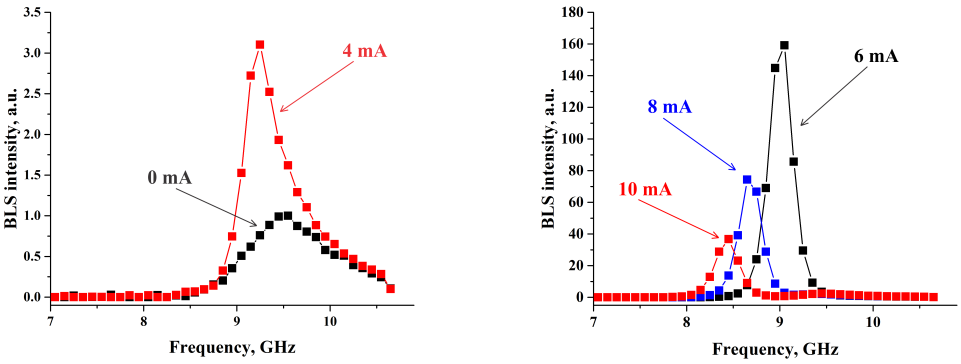

(a) (b)

Figure 5.3: (a) and (b) BLS spectra of the magnetization oscillations in the Py layer measured at the labeled current values. Symbols are experimental values, curves are guides for the eye.

All this information is collected in Figure 5.4a. It is a logarithmic color-coded map, which shows the intensity of the BLS spectrum as a function of the driving current and frequency. The right lobe is associated with thermally exited magnons which always exist at finite temperatures. The left one, which appears at $I \approx 5$ mA (white dashed line in the figure), corresponds to the auto-oscillation mode. Figure 5.4b shows the dependence of the integral BLS intensity on the current. It abruptly increases at $I > 5$ mA marking the onset of auto-oscillations as discussed in the second chapter. In order to find the critical current I_c more precisely, we also plotted the inverse of integral BLS intensity in the same graph. By extrapolating the dependence, we estimated $I_c = 5.4$ mA.

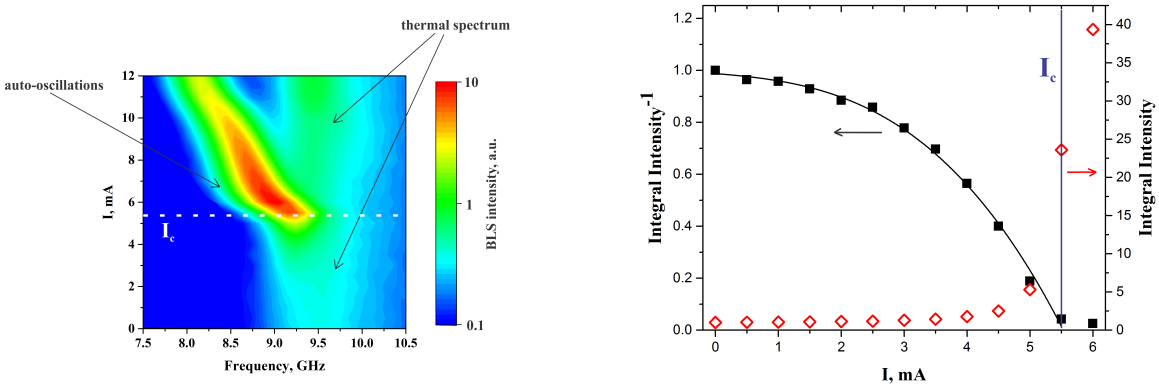

(a) (b)

Figure 5.4: (a) Color-coded map of the measured BLS intensity in the current-frequency coordinates, white dashed line shows the critical current I_c. (b) Integral intensity (diamonds) and its inverse value (squares) vs. current. The dependencies are normalized by the value $I = 0$. I_c marks the threshold current for the onset of auto-oscillations. Curve is the result of the polynomial fitting.

5.2 Electronic measurements

When the driving current exceeds the critical value I_c, the auto-oscillation amplitude becomes sufficiently large, and electronic signals generated in the antenna can be detected by the spectrum analyzer. Figure 5.5 shows an example of measured electronic spectrum. As discussed in the second chapter, in order to precisely determine the central frequency f_c and the FWHM Δf, one should fit the detected peaks with a Lorentzian function [46].

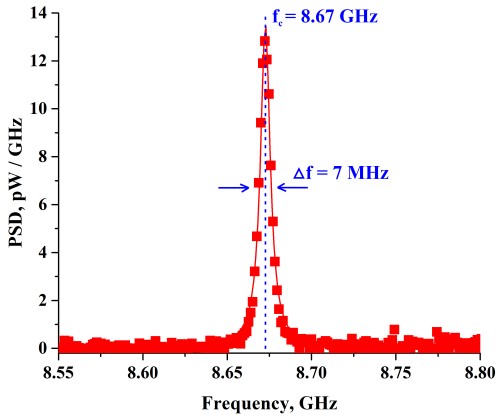

Figure 5.5: Spectrum of the electronic signal induced by the nano-oscillator measured at $I = 8$ mA and $H_0 = 1000$ Oe. Symbols are experimental data, curve is the result of fitting by the Lorentzian function.

To understand how the driving current affects the operation frequency f_c and the spectral linewidth Δf we performed measurements at different I. Figure 5.6a shows a color map of the power spectral density (PSD) of the measured electronic signals in the current-frequency coordinates. The data demonstrate that the oscillations can be detected only at $I > 6$ mA. Additionally, it is seen that the NLSI-based oscillator exhibits single-frequency auto-oscillation with narrow spectral linewidth within the entire studied current range up to 10 mA. The coefficient of the nonlinear frequency shift N in the case of an in-plane magnetic field is negative, and therefore the central frequency f_c of the spectral peaks decreases with increasing current. Figure 5.6b shows good agreement between the operation frequencies f_c measured by means of microwave spectroscopy (blue solid line) and the BLS technique (red diamonds).

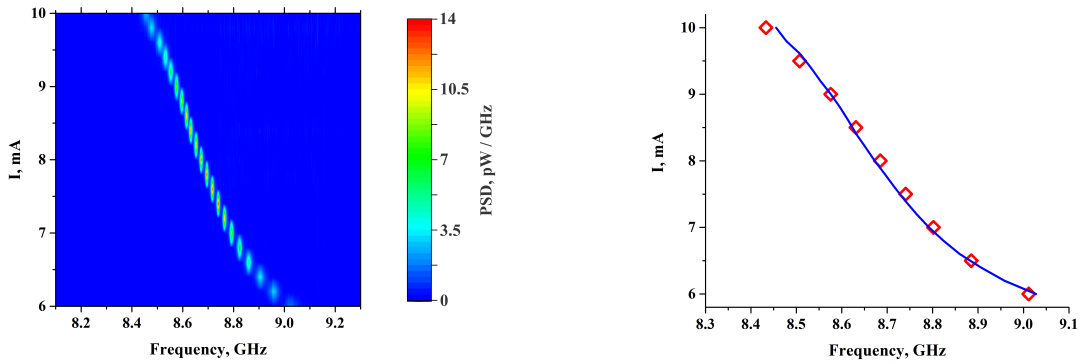

Figure 5.6: (a) Color map of the power spectral density of the electronic signal vs. current and frequency. (b) Center frequency f_c as a function of the driving current I measured by electronic microscopy (blue solid line) and BLS (red diamonds).

At the beginning of this chapter we have mentioned the limited frequency resolution of BLS spectroscopy, which didn't allow to measure precisely the spectral linewidth of the NLSI-based oscillators in the previous study [36]. But microwave spectroscopy is free from this limitation. Figure 5.7 shows the dependence of the linewidth Δf on the driving current I. At first, it decreases rapidly for current above I_c, then it reaches the broad minimum of 7 MHz at 7.5 mA and finally starts to increase at $I > 9$ mA. This behavior is correlated with that of the peak power (filled symbols in Figure 5.7). The latter firstly rapidly increases after the onset of auto-oscillations, saturates at 7.5 mA and subsequently decreases at large currents. In order to interpret the measured dependencies, we additionally plotted the integral power of the electronic signals as a function of the current I in Figure 5.8.

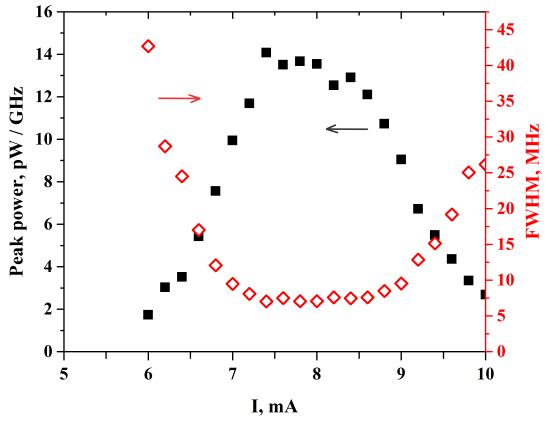

Figure 5.7: Peak power (filled squares) and spectral linewidth (open diamonds) vs. current. The data were measured at $H_0 = 1000$ Oe.

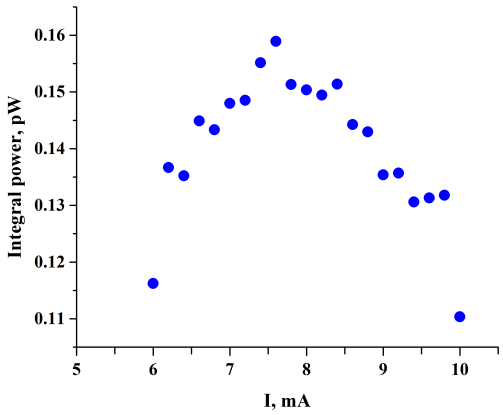

Figure 5.8: Current dependence of the integral power of the electronically detected signals. The data were measured at $H_0 = 1000$ Oe.

From theory [46] we know that the generation linewidth Δf is inversely proportional to the energy of oscillations. As follows from Figure 5.8, the integral power of measured signal increases at currents above I_c, and consequently the observed linewidth narrows (Figure 5.7). But the auto-oscillations amplitude can not grow forever, it should be limited by the nonlinear effects. As a result Δf reaches its minimum at 7.5 mA. However, as can be seen in Figure 5.7, the further increase in current leads to spectral broadening. This behavior can be explained by nonlinear coupling of the auto-oscillation mode with other magnetic modes of the system. In [26] it was shown that the spin-transfer torque disproportionately enhances the amplitudes of long-wavelength modes and thus creates a nonequilibrium spin-wave distribution. As a result, that leads to nonlinear magnon-magnon interactions and redistribution of the energy within the magnon spectrum. This conjecture is supported by a fact that the auto-oscillation frequency monotonically decreases (Figure 5.6b), even when the integral power of the detected peaks starts to decrease (Figure 5.8) at $I > 8$ mA. The nonlinear frequency shift is determined by the energy stored in all the magnetic modes. Thus, the behaviors observed at large currents indicate that the energy is transferred from the auto-oscillation to the dynamic magnetic modes which cannot be directly detected in the experiment due to their short wavelengths.

The data presented in Figure 5.7 and 5.8 were measured at $H_0 = 1000$ Oe, but similar results were obtained for other values of the external field. It was found that the minimal linewidth slightly increases with increasing H_0, as illustrated by three electronic spectra in Figure 5.9 measured at $H_0 = 600$ Oe, 1000 Oe and 1400 Oe respectively. Both the center frequency f_c and the spectral linewidth Δf as functions of the field H_0 are shown in Figure 5.10. It demonstrates that the frequency of the NLSI nano-oscillator can be tuned over a wide range while the minimum linewidth remaining at a few megahertz.

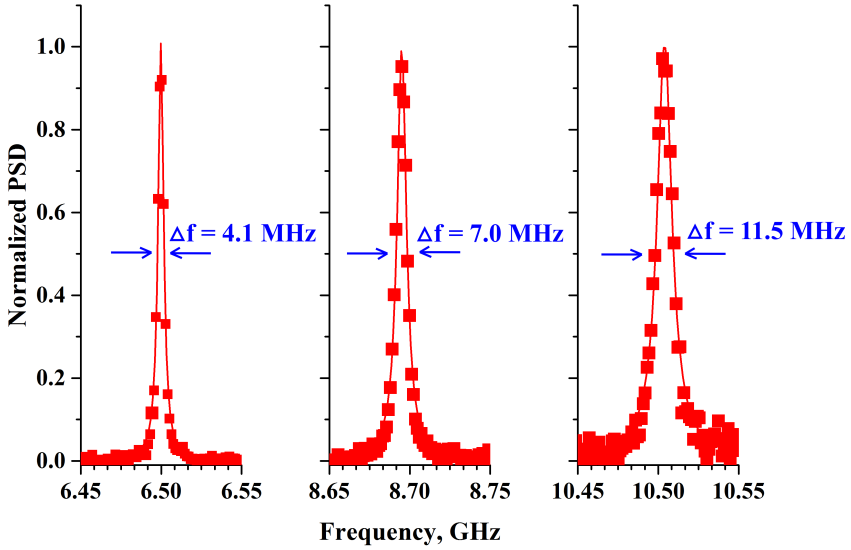

Figure 5.9: Spectra of the measured electronic signals generated by the NLSI-based oscillator at $H_0 = 600$ Oe, $H_0 = 1000$ Oe and $H_0 = 1400$ Oe, respectively. Curves are the result of fitting by the Lorentzian functions.

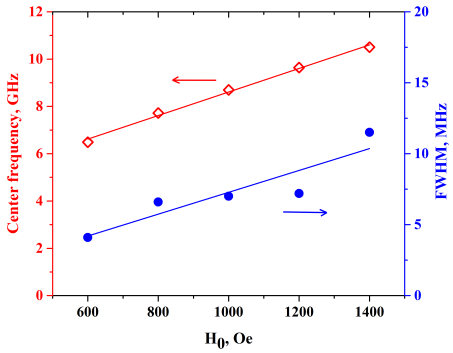

Figure 5.10: Dependence of the central frequency f_c and the spectral linewidt Δf on the external magnetic field H_0. Symbols are experimental values, lines are guides for the eye.

5.3 Conclusions

Presented results shed light on the spectral characteristics of the magnetic nano-oscillators driven by pure spin currents generated by the nonlocal spin injection mechanism. At first, by using micro-focus BLS spectroscopy we estimated the spatial size of the auto-oscillations mode. As in the previous case [36] it exceeds 300 nm in the diameter. Also due to the high sensitivity

of the BLS technique we managed to study the magnetization dynamics before the onset of auto-oscillations. As a result we found the value of critical current $I_c = 5.4$ mA for our system. Then we used electronic microwave spectroscopy to achieve the high spectral resolution of measurements and precisely determine the linewidth of the NLSI-based oscillators. We showed that the devices exhibit highly coherent dynamics with the spectral linewidth of a few megahertz at room temperature. For example, the FWHM reaches 4 MHz at $H_0 = 600$ Oe. Finally, we established that the coherence is preserved over a broad range of the external field.

Chapter 6

Excitation of propagating spin waves by nonlocal spin injection

In previous two chapters we have discussed the advantages of the NLSI-based oscillators, namely the minimized Joule heating effects and the narrow spectral linewidth. However, so far only spatially localized auto-oscillations have been excited in these devices [36], and therefore they cannot be used as sources of propagating spin waves in magnonics circuits, for example. Actually the excitation of spin waves is an important issue in modern magnonics because the traditional inductive method becomes inefficient on the nanoscale [11]. In this chapter we demonstrate a device which exhibits efficient excitation and directional propagation of coherent spin waves with a large propagation length.

Sketch of the studied structure is shown in Figure 6.1, and it consists of two subsystems. The first one is a familiar three-layer structure Py(5)Cu(20)CoFe(8), which properties we have discussed in the previous chapters. We will call it an active subsystem because here the localized auto-oscillation mode is excited (see Section 2.4 for details) with the spatial size of about 300 nm (Figure 5.2). To convert these localized oscillations into a propagating spin wave, a waveguide (the second subsystem) is placed on top of the Py film. The distance between the nanocontact and the waveguide edge was chosen 150 nm to ensure efficient coupling between two subsystems.

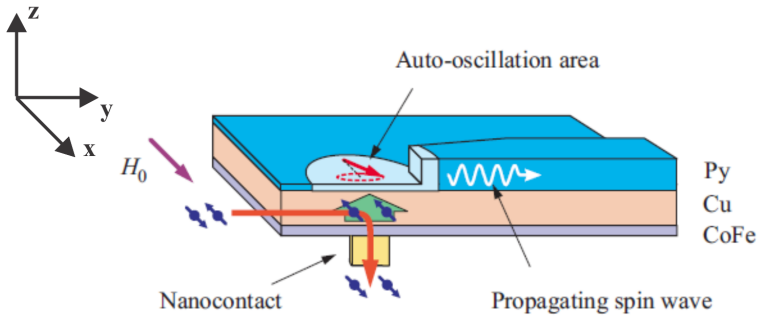

Figure 6.1: Sketch of the proposed device.

6.1 Waveguide optimization

As we have mentioned in Chapter 2, because of finite size of a ferromagnetic sample uncompensated magnetic surface charges emerge on its surface. As a result, they produce the demagnetizing field $\mathbf{H}_{dem}$ directed oppositely to the external field $\mathbf{H}_0$ (Figure 6.2). Thus the internal field $\mathbf{H}_{int} = \mathbf{H}_0 + \mathbf{H}_{dem}$ decreases inside the sample. For calculations of the demagnetizing and the internal fields we used the Mumax3 software [62].

Figure 6.2 shows the simplest form of the waveguide subsystem. It is a 20 nm thick and 500 nm wide Py stripe placed on top of the 5 nm thick Py film. During this section other layers are unimportant. The external field $\mathbf{H}_0 = 1000$ Oe is directed along the x-axis. Figure 6.3a demonstrates a calculated distribution of the x-component of the demagnetizing field $\mathbf{H}_{dem}$ across the waveguide. As expected it is directed anti-parallel with $\mathbf{H}_0$ (notice negative values) and therefore reduces the internal field inside the waveguide.

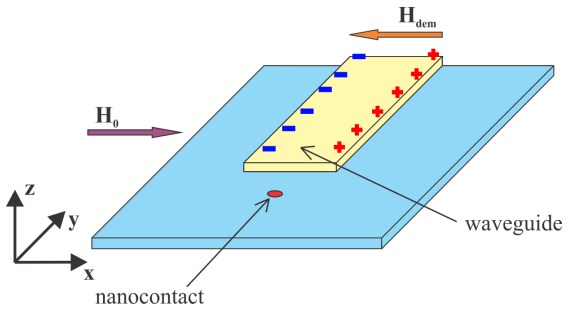

Figure 6.2: Rectangular-shaped Py waveguide (yellow colored) placed on top the Py film (blue colored). The Cu and CoFe layers are not shown.

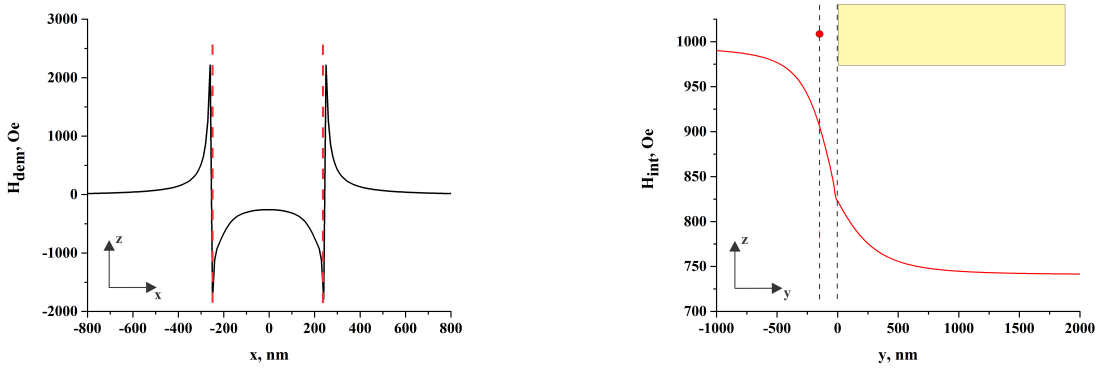

(a) **(b)**

Figure 6.3: (a) Calculated distribution of the demagnetizing field in the waveguide along the x-axis. Two vertical dashed lines mark the edges of the stripe. (b) Calculated profile of the x-component of the internal field along the y-axis. Left and right vertical lines show the positions of the nanocontact and the waveguide, respectively. The data were calculated at $\mathbf{H}_0 = 1000$ Oe.

Figure 6.3b shows a calculated spatial profile of the x-component of the internal field $\mathbf{H}_{int}$ along the y-axis. Far outside the waveguide the field is equal to the external value 1000 Oe. But due to the demagnetizing effects, it starts decreasing near the edge and finally reaches a value about 750 Oe inside the waveguide. This slow variation leads to two undesirable effects. But before we discuss them, we should consider a general problem of spectral matching between the spin-torque nano-oscillator and the magnonic nano-waveguide.

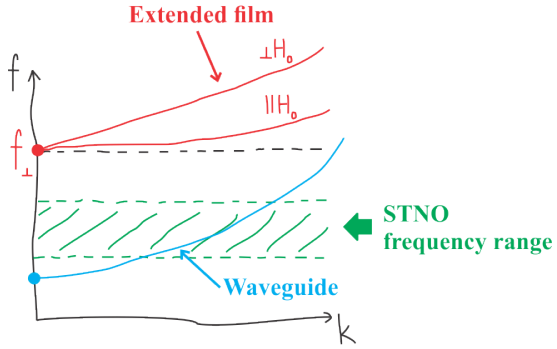

Figure 6.4: Schematic hand-drawn picture of spin-wave dispersion relations. Two red curves correspond to spin waves propagating in the extended Py film parallel and perpendicularly to the external field $\mathbf{H}_0$. The blue curve is the dispersion law for the waveguide mode. The green shaded area shows operating frequency range of the spin-torque nano-oscillator.

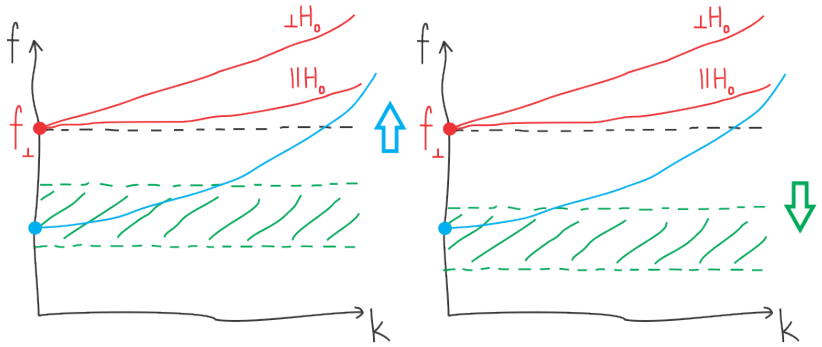

Figure 6.5: (a) Local reduction of the internal field near the edge of the stripe results in upward shift of the waveguide dispersion curve. (b) Decrease of the magnetic field in the vicinity of the nanocontact leads to downward shift of the STNO frequency range.

In hand-drawn Figure 6.4 the red curves schematically represent the dispersion relations $f(k)$ for spin waves in the extended 5nm thick Py film propagating perpendicular ($\perp\mathbf{H}_0$) and parallel ($\|\mathbf{H}_0$) to the direction of the external magnetic field. They both start at the frequency of the

uniform ferromagnetic resonance (FMR, Kittel formula [66]):

$$f_{\perp} = \gamma\sqrt{H_0(H_0 + 4\pi M_0)} \tag{6.1}$$

and then monotonically increase with growing wavevector k. These curves can be calculated by using the well developed analytical theory [67, 68]. In the previous chapter we have seen that by changing the bias current I, we can tune the the operation frequency of the NLSI-based nano-oscillators in a wide range (Figure 5.10). But as shown in Figure 5.8 the devices generate intense microwave signals only for current above 6mA and below 10mA. For $I < I_c = 5.4$mA the spin-transfer torque doesn't completely compensate the natural magnetic damping and therefore auto-oscillations are not possible. For $I > 10$mA the integral power of oscillations becomes too small due to nonlinear scattering processes. In other words, this current band defines the frequency range of the NLSI-based oscillators (shown as green shaded area in Figure 6.4). The range lies entirely below the FMR frequency $f_{\perp}$ and therefore doesn't intersect with the dispersion curves for the extended magnetic film (red color in the figure). As a result the auto-oscillation mode is spatially localized and doesn't radiate spin waves in the surroundings film. Finally the blue curve in Figure 6.4 is the dispersion law for spin waves propagating in the waveguide. It can be also calculated analytically but only with approximations [11], and therefore one usually uses micromagnetic simulations to find it (we will discuss one of the methods in section 6.3).

Figure 6.4 shows good spectral matching since the dispersion spectrum of the waveguide mode overlaps with the entire STNO frequency range. In other words, for every auto-oscillation frequency there is a propagating spin wave with the same frequency and nonzero wave vector k. But in the case of the regular stripe (Figure 6.2) there are two unwanted effects, which prevent efficient spectral matching. At first, the internal field increases significantly near the edge of the waveguide (Figure 6.3b). As a result, the waveguide dispersion curve is locally shifted to higher frequencies (Figure 6.5a), and consequently spectral matching becomes worse. Additionally, the external field $\mathbf{H}_0$ is reduced at the position of the nanocontact (Figure 6.3b), and therefore the entire frequency range of the nano-oscillator shifts downwards (Figure 6.5b). Eventually the system exhibit poor spectral matching, which prevents efficient excitation of propagating spin waves. So we can conclude that instead of smooth variation the internal field should have more abrupt profile across the edge of the waveguide, ideally it should be a step function. And one can try to achieve it, by modifying the waveguide configuration.

Firstly, the waveguide can be tapered. For example, the width can be changed from 500 nm to 300 nm at the edge (Figure 6.6a). It is known that in narrower stripes the demagnetizing field $\mathbf{H}_{dem}$ is more intense because the effective magnetic charges are located closer to each other [42]. As a result, the internal field is more decreased in the constriction region (Figure 6.6b), and therefore its profile becomes steeper near the edge of the waveguide. However, the magnetic field is still reduced at the location of the nanocontact.

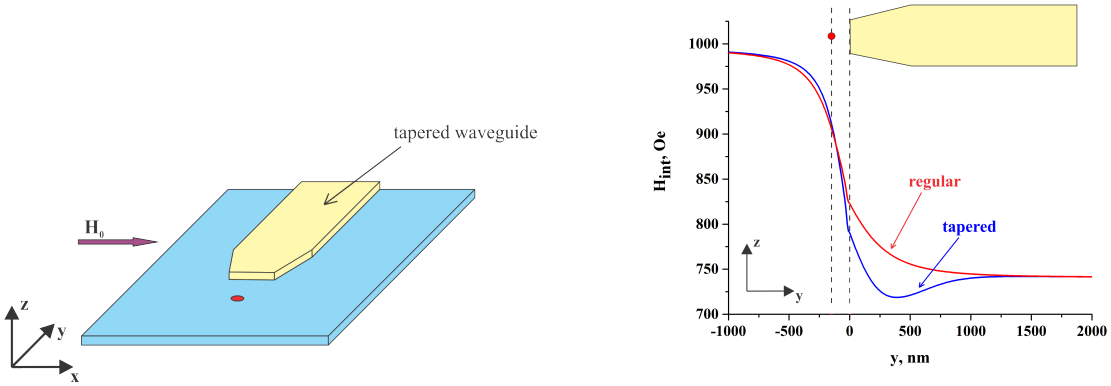

(a) (b)

Figure 6.6: (a) Schematic picture of the tapered waveguide. (b) Calculated distribution of the internal magnetic field along the y-axis for the regular (red) and the tapered (blue) waveguides. The data were calculated at $\mathbf{H}_0 = 1000$ Oe.

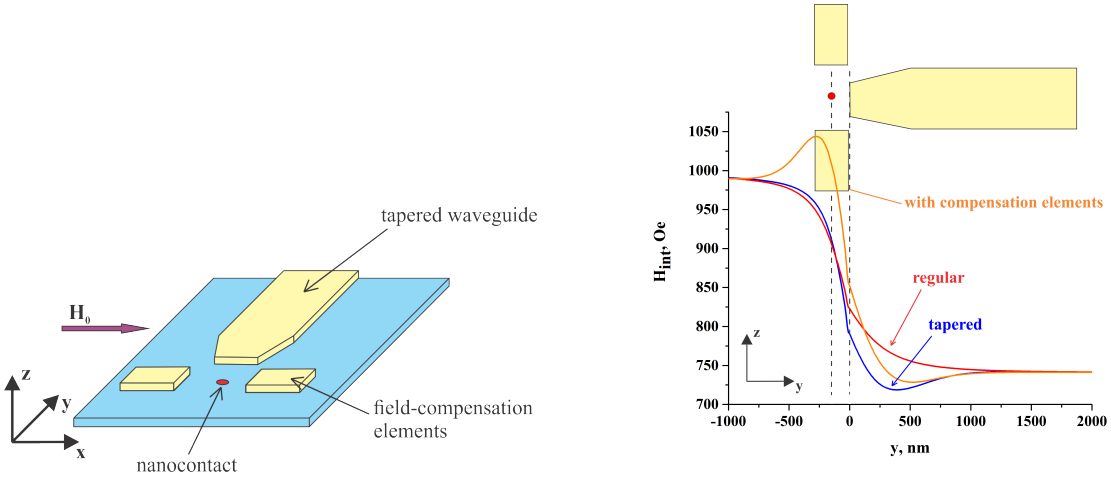

(a) (b)

Figure 6.7: (a) Schematic picture of the tapered waveguide with additional field-compensation elements. (b) Calculated distribution of the internal magnetic field along the y-axis for the regular (red) and the tapered (blue) waveguides. The orange curve shows the configuration with additional elements. The data were calculated at $\mathbf{H}_0 = 1000$ Oe.

Next we can add some extra elements. For example, two Py rectangles with widths of 500 nm, lengths of 300 nm and 20 nm thicknesses (Figure 6.7a). Each of them creates the demagnetizing field with the same distributions as a regular rectangular stripe (Figure 6.3a). As can be seen in Figure 6.3a, outside the element $\mathbf{H}_{dem}$ is directed along the the x-axis (notice positive values), and thus it locally increases the external magnetic field. Contributions from both elements add

together and give rise to the distribution of the internal field shown in Figure 6.7b. Now the magnetic field in the vicinity of the nanocontact is equal to the external field.

Actually we can further improve the structure. For instance, instead of rectangular elements one can use triangles (Figure 6.8a), the corresponding internal field distribution is shown in Figure 6.8b. However, the benefits are not so significant, and therefore in the experiment we investigated the systems with rectangular elements.

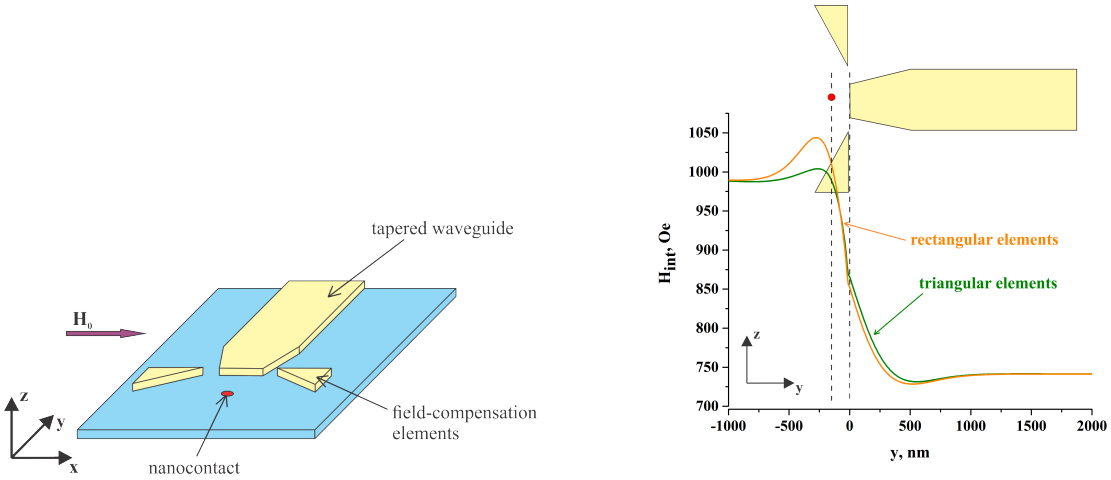

(a) (b)

Figure 6.8: (a) Schematic picture of the tapered waveguide with triangular field-compensation elements. (b) Calculated distribution of the internal magnetic field along the y-axis for the waveguide with rectangular (orange) and triangular (green) additional elements. The data were calculated at $\mathbf{H}_0 = 1000$ Oe.

6.2 Experiment

Experimentally the current-induced magnetization dynamics was investigated by means of micro-focus BLS spectroscopy [57]. Figure 6.9 shows an atomic-force microscopy (AFM) image of the studied device. The waveguide of the width 500 nm was tapered to 300 nm at the edge, the additional elements with dimensions of 500 nm by 300 nm were separated by 500 nm from edge to edge. All the elements were 20 nm thick and made from Py. The external field $\mathbf{H}_0$ was applied across the waveguide, along the x-axis.

At first, we located the probing laser spot on extended part of the Py film, set the driving current to zero $I = 0$ and measured spectra of the magnetization dynamics induced by thermal fluctuations for different values of the external field $\mathbf{H}_0$. Figure 6.10a shows an example of the recorded spectrum.

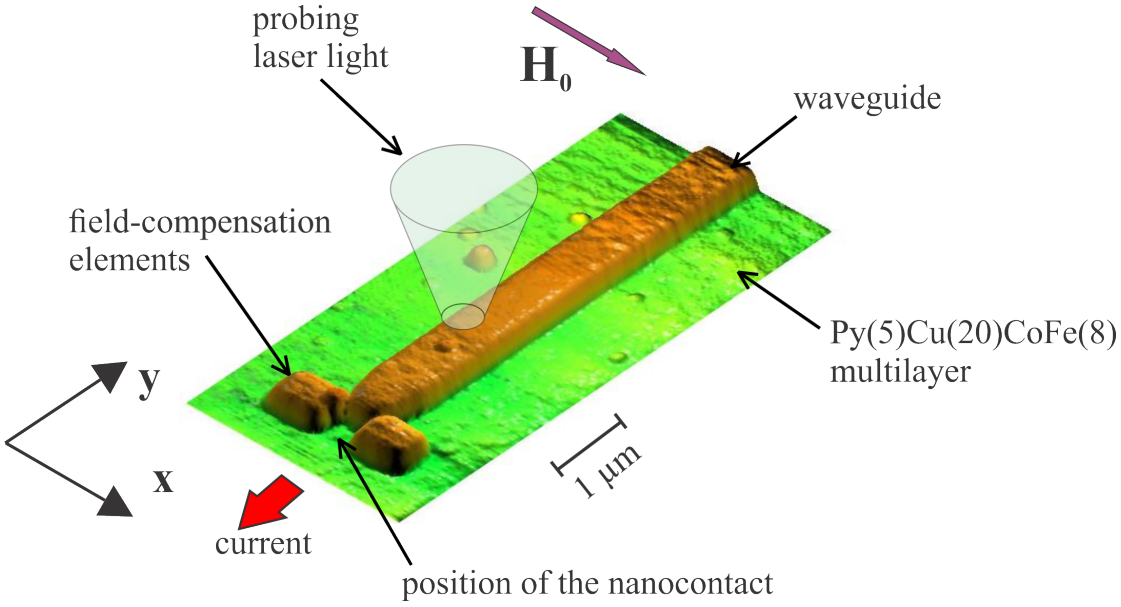

Figure 6.9: AFM image of the device.

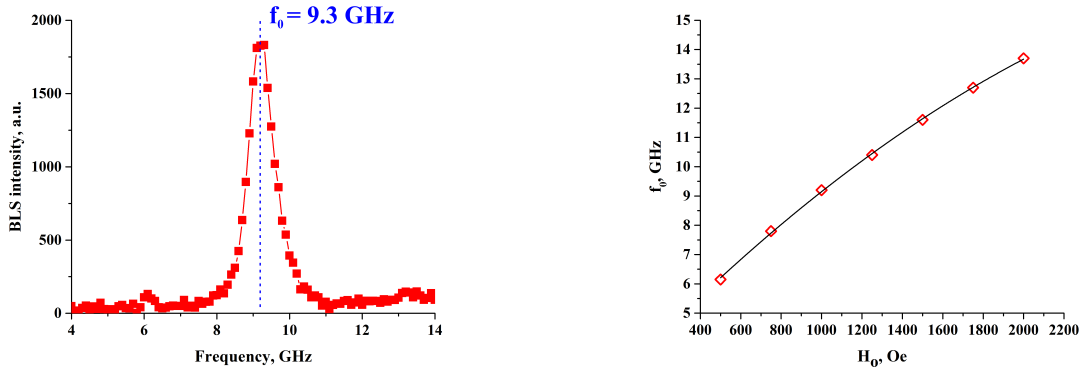

(a) **(b)**

Figure 6.10: (a) Spectrum of thermally excited magnons at $\mathbf{H_0} = 1000$ Oe. (b) FMR frequency f_0 as a function of H_0. Red diamonds are measured values, black curve is the result of the fitting based on the Kittel formula.

The central frequency of the peak f_0 can be associated with the frequency of the uniform ferromagnetic resonance (section 4.3.2 in [58]). Figure 6.10b shows the dependence of f_0 on the external field magnitude H_0. By fitting the experimental data with the Kittel formula (6.1), we can find the saturation magnetization $4\pi M_0$, and in our case it is equal to 9.8 kG. We will need this material parameter for micromagnetic simulations.

Next we placed the probing laser spot directly at the position of the nanocontact to investigate the magnetization dynamics of the NLSI-based oscillator. At small applied currents only the

magnetization oscillations induced by thermal fluctuations are observed (like in Figure 6.10a). With increasing I they become more intense, and at certain critical value I_c the transition to the auto-oscillation regime happens. In order to estimate the critical current, we used the same method described in Chapter 5, and we found $I_c = 3.6$ mA. Figure 6.11 shows the measured BLS spectra at different the currents above I_c. As can be seen the auto-oscillation frequency always lies below the FMR frequency f_0, and therefore the excited mode is spatially localized and doesn't radiate spin waves into the surrounding film.

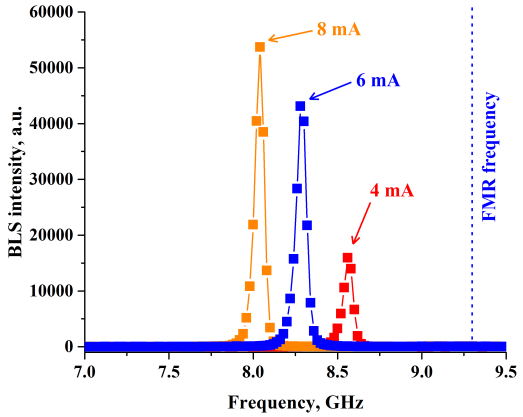

Figure 6.11: BLS spectra (symbols) measured at different I. Curves are guides for the eye, the vertical line marks the FMR frequency $f_0 = 9.3$ GHz. The data were measured at $\mathbf{H}_0 = 1000$ Oe.

After the preliminary part we studied excitation of propagating spin waves. For that we scanned a rectangular 4 μm by 1.2 μm area around the nanocontact by the probing laser spot. A spatial map in Figure 6.12 shows the distribution of the local intensity of the dynamic magnetization, which looks like a comet. The "head" is a high-intensity region around the nanocontact, which represents the localized auto-oscillation mode induced by pure spin currents. The extended "tail" is an excited spin wave propagating along the waveguide. To prove that the spin wave is concentrated in the waveguide and doesn't radiate its energy into the surrounding film, we plotted the transverse section of the intensity map (Figure 6.13). As can be seen, the measured intensity is almost entirely confined to the waveguide. This observation confirms the directional propagation of the excited spin wave.

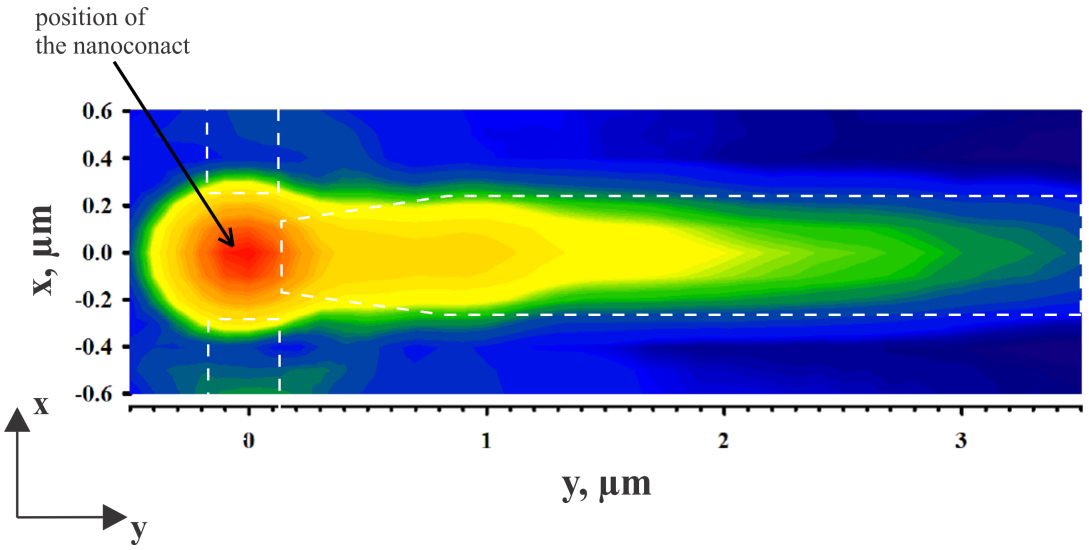

Figure 6.12: Normalized color map of the BLS intensity for a region around the nanocontact. White dashed lines mark the waveguide and the field-compensation elements. The data were measured at $I = 4$ mA and $\mathbf{H}_0 = 1000$ Oe.

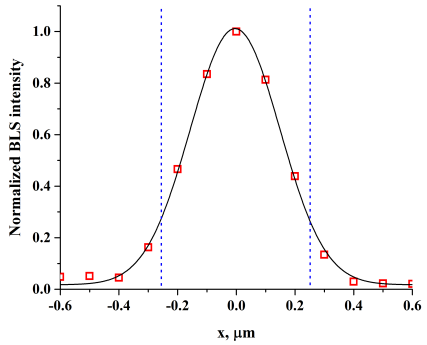

Figure 6.13: Transverse section of the intensity map at the distance of 2 μm from the nanocontact. Symbols are measured values, black curve is the Gaussian fit. Two vertical dashed lines show the lateral edges of the waveguide. The data were obtained at $I = 4$ mA and $\mathbf{H}_0 = 1000$ Oe.

For integration of the studied device into magnonic circuits it should exhibit sufficiently large propagation length l. By definition it is the distance over which the spin wave amplitude decreases by a factor of $e = 2.71....$ In order to find l, we plotted the BLS intensity as a function of the propagation distance y in Figure 6.14a. Note that the data are plotted on the logarithmic scale, therefore the observed linear decrease is actually an exponential decay $exp(-2x/l)$. By fitting the data we find that the propagation length is equal to 3μm in our case. It is large enough for possible technical applications of the devices.

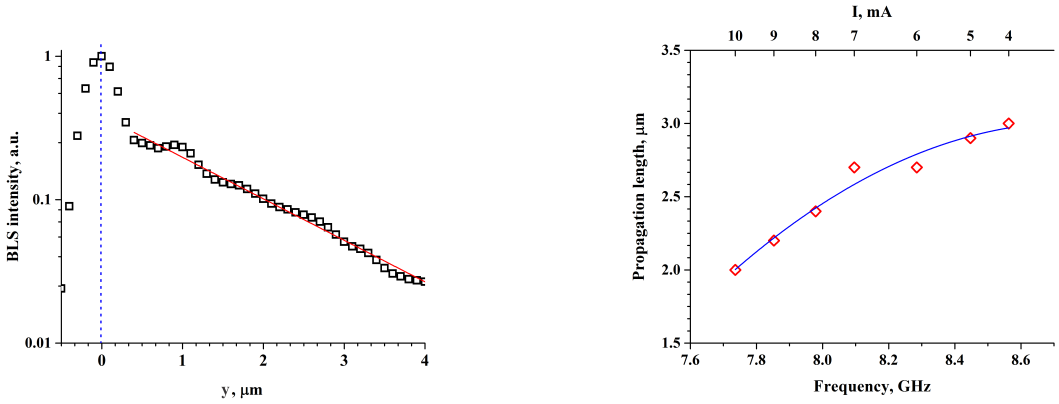

(a) (b)

Figure 6.14: (a) Dependence of the BLS intensity on the propagation coordinate y. Symbols are experimental data, red line is the result of linear fitting. Vertical line marks the position of the nanocontact. The data were obtained at $I = 4$ mA and $\mathbf{H}_0 = 1000$ Oe. (b) Propagation length l as a function of the auto-oscillation frequency (bottom scale) and the driving current I (top scale). Symbols are measured values, curve is guide for the eye.

By performing similar measurements for different driving currents, we found that the propagation length decreases with increasing I (Figure 6.14b, top horizontal scale). As we will show below, this decrease is associated with the decreasing frequency of auto-oscillation (bottom horizontal scale in Figure 6.14b). In order to prove that we performed micromagnetic simulations.

6.3 Micromagnetic simulations

Initially, our goal was to calculate the dispersion relation $f(k)$ for the waveguide mode. For that we used the MuMax3 software [62], the script can be found in the appendix. The first step is to define the geometry. Because we were interested only in the propagation of spin waves, not in their excitation, we didn't take into account the waveguide's finite length and the field-compensation elements. Instead we investigated a structure shown in Figure 6.15. It is a 12μm $\times$ 3μm $\times$ 5 nm Py base (blue colored) and a 12μm $\times$ 500 nm $\times$ 20 nm Py waveguide (yellow colored) on the top of it. Entire system was discretized into 100 $\times$ 10 $\times$ 5 nm^3 cells. In the calculations we used the standard Gilbert damping constant $\alpha = 0.01$ and the exchange stiffness $A_{ex} = 1.3 \cdot 10^{-11} J/m$. The saturation magnetization $4\pi M = 9.8$ kG we had determined beforehand from the BLS measurements (Figure 6.10b).

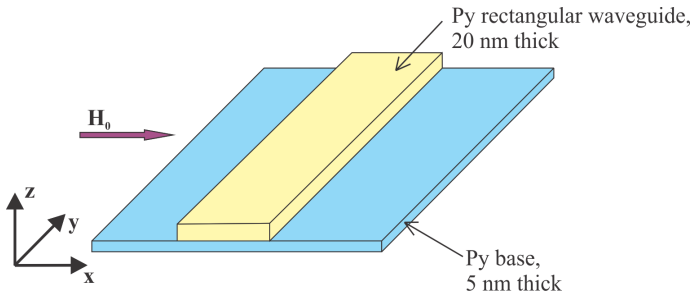

Figure 6.15: Schematic picture of the studied system.

After we defined the geometry and material parameters, we used periodic boundary conditions (PBC) along the y-axis and found the ground state of the system. PBC help us to get rid of undesirable boundary domains (Figure 6.16) and since the waveguide is much longer than the propagation length of the spin waves, such simplification is acceptable. The external field $\mathbf{H}_0 =$ 1000 Oe was directed along the x-axis.

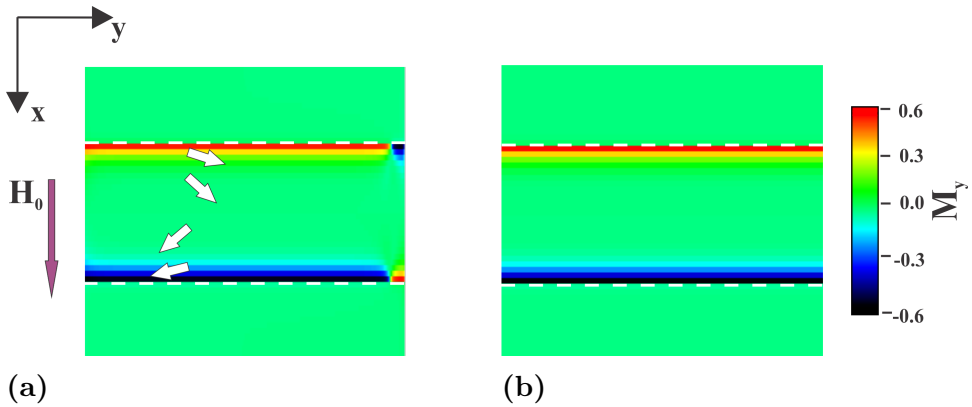

Figure 6.16: Color-coded maps of the y-component M_y without (a) and with (b) periodic boundary conditions. Two horizontal lines mark the edges of the waveguide. Small white arrows show the local direction of the magnetization.

Next step is to excite spin waves and find the dispersion law $f(k)$. Generally speaking there are several methods, and we chose the following: we added to the static homogeneous field $\mathbf{H}_0 = H_0\mathbf{e}_x$ an imhomogeneous perturbation $\delta\mathbf{H}(\mathbf{x},\mathbf{y},\mathbf{t}) = A(t)H_x(x)H_y(y)\mathbf{e}_x$.
The time-dependent amplitude is given by

$$A(t) = a \cdot \frac{sin(2\pi f_{max}t)}{2\pi f_{max}t},$$

where a and f_{max} are parameters. It is a sinc function, and its Fourier transform is a rectangular function. Therefore it allows us to excite all frequencies in a range from 0 to f_{max}. We used $a = 1$ Oe and $f_{max} = 20$ GHz.
The y-dependent part is

$$H_y(y) = cos(\frac{2\pi N_y}{L_y}),$$

where L_y is the waveguide length (12μm in our case) and N_y is a parameter, which defines number of wavelengths per L_y. Figure 6.17 shows $H_y(y)$ profiles for different N_y.

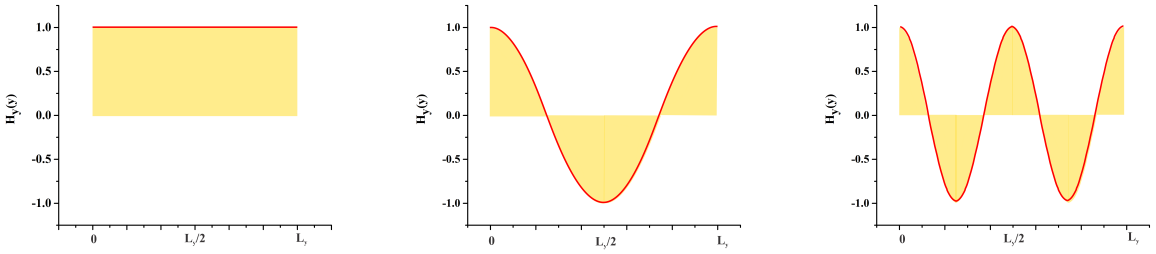

(a) **(b)** **(c)**

Figure 6.17: (a) - (c) $H_y(y)$ profiles for $N_y = 0, 1$ and 2, respectively.

If we fix N_y, we will excite a spin-wave with a predefined wavelength $\lambda = \frac{L_x}{N_y}$ or wavenumber $k = \frac{2\pi N_y}{L_x}$ (Figure 6.18). Then by using Fourier analysis, we can find a frequency corresponding to this mode. Thus by gradually changing $N_y = 0, 1, ...$, we can compute the entire dispersion relation $f(k)$.
Finally the x-dependent part is just a rectangular function

$$H_x(x) = \begin{cases} 0, \text{ if } x < -\frac{w}{2} \\ 1, \text{ if } -\frac{w}{2} < x < \frac{w}{2} \\ 0, \text{ if } x > \frac{w}{2} \end{cases} ,$$

where w is the stripe width (500 nm in our case). In other words the perturbation $\delta H(x, y, t)$ is non-zero only inside the waveguide.

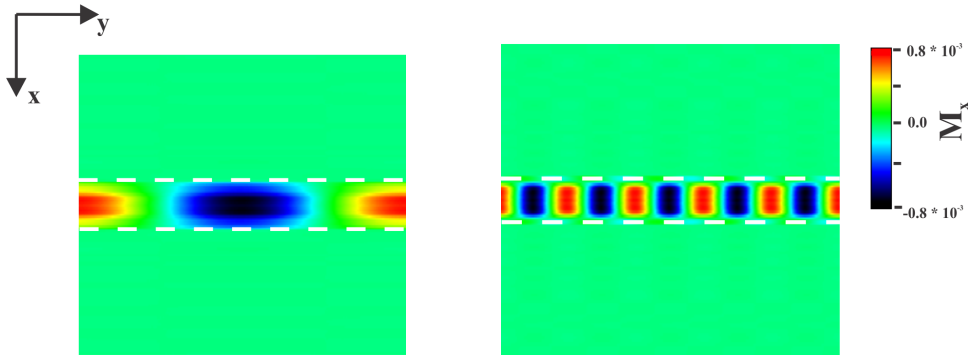

(a) **(b)**

Figure 6.18: Calculated distributions of the y-component M_y for two different wavelengths (a) $N_y = 1$ and (b) $N_y = 5$. Two horizontal lines mark the waveguide edges.

After we defined the excitation, we performed simulations. Figure 6.19 demonstrates the calculated dispersion relation $f(k)$ (blue symbols). The lowest frequency is equal to 7.5 GHz, and it is

below the smallest auto-oscillation frequency of the nano-oscillator. In other words, the waveguide supports propagation of spin waves at all frequencies within this frequency range. The red curves are dispersion characteristics of spin waves propagating in the extended Py film, calculated by using the analytic theory [67]. They both start at the FMR frequency of 9.2 GHz. If the frequency of spin wave exceeds this value, it is no longer confined in the waveguide and propagates through the extended film instead.

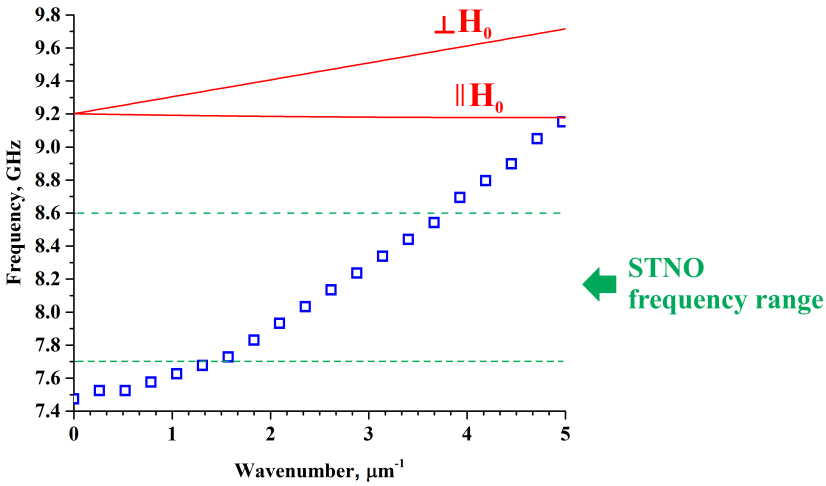

Figure 6.19: Symbols are calculated dispersion $f(k)$ for spin waves propagating in the waveguide. Two red curves are dispersion relations for spin waves propagating in the extended 5 nm thick Py film perpendicularly and parallel to the external magnetic field. Green horizontal lines show boundaries of the frequency range of the nonlocal oscillator.

Also the simulations allowed us to calculate the propagation length l. For that we used an analytical formula (p.167 in [5])

$$l = \frac{v_{gr}}{\alpha\omega\frac{\partial\omega}{\partial\omega_H}},$$

where $v_{gr} = \frac{\partial\omega}{\partial k}$ is the spin wave group velocity and $\omega_H = \gamma H_0$. Figure 6.20 shows the results of calculations. They reproduce the experimentally observed decrease of the propagation length with decreasing auto-oscillation frequency (Figure 6.14b). The possible explanation is the reduction of the group velocity at smaller frequencies. It can be seen from the decreasing slope of the dispersion curve in Figure 6.19. Finally, the calculated values are in good quantitative agreement with the experimental data.

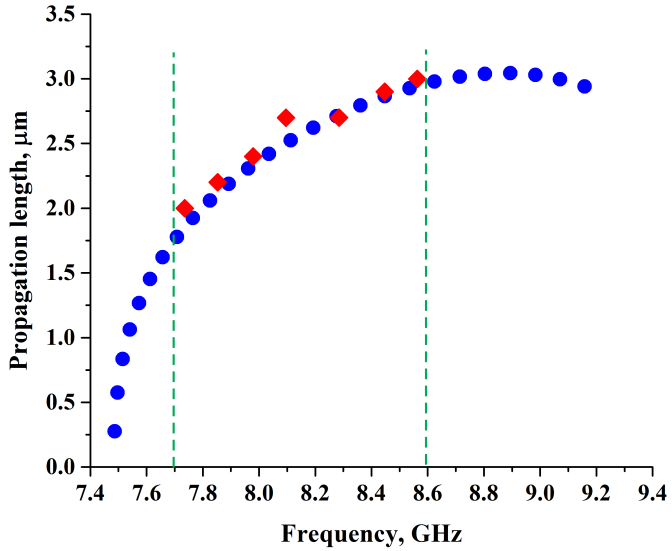

Figure 6.20: Propagation length vs. frequency. Blue circles are calculated values, red diamonds are experimental results. Two vertical lines show the frequency range of the nano-oscillator. The data were obtained at $H_0 = 1000$ Oe.

6.4 Conclusions

In this chapter we demonstrated that directionally propagating spin waves can be efficiently excited by pure spin currents generated by the nonlocal spin-injection mechanism. At first, we showed that good spectral matching between the nano-oscillator and the magnonic nano-waveguide can be achieved, by utilizing the demagnetizing field effects. Then, by means of the BLS technique, we investigated the current-induced magnetization dynamics and observed the excited spin waves. We showed that they are confined in the waveguide and therefore propagate directionally. Also we demonstrated that the studied system exhibits sufficiently large propagation length. Finally, we performed micromagnetic simulations, which helped us to understand mechanisms controlling the spin-wave propagation in the device. The results of calculations are in good quantitative agreement with the experimental data. We believe that the demonstrated results open new perspectives for the future-generation electronics such as spintronics and magnonics.

Chapter 7

General conclusions and outlook

In this thesis we investigated features of a new type of spin-torque nano-oscillators. The operation principle of the studied devices are based on the nonlocal spin injection mechanism, which allow one to make use of all the advantages of pure spin currents.

First of all, it was shown in Chapter 4 that nonlocal oscillators exhibit negligible flow of the electrical current through the active magnetic layer and do not suffer from the detrimental effects of layers with strong spin-orbit coupling on the dynamic magnetic damping. Moreover, since the driving current in the NLSI devices flows mostly through low-resistivity layers, the Joule heating effects are minimized. In particular, our heat flow simulations show that the maximal temperature increase in the active device region does not exceed 10 K within the range of currents used in the experiments.

Secondly, in Chapter 5 we presented spectroscopic measurements, which directly demonstrate the high coherence of nano-oscillators driven by nonlocal spin injection. We showed that the devices exhibit auto-oscillations with the spectral width of a few megahertz at room temperature. For example, the linewidth reaches 4 MHz at the operation frequency of 6 GHz. In addition the coherence is preserved over a broad range of the external magnetic field, and that allows the wide-range frequency tunability.

Finally, we demonstrated that propagating spin waves can be generated by means of the NLSI mechanism. We experimentally showed that the excited spin waves propagate directionally with sufficiently large propagation length about $3\mu m$. All these features make the NLSI oscillators promising candidates for applications in the future-generation electronics.

As one can see from this summary, during this thesis many properties of the nonlocal oscillators have been studied, but for a full understanding of the current-induced dynamics further researches are needed. At first, reasons of the large size of the excited auto-oscillation mode should be clarified. It exceeds 300 nm in diameter, and that can't be explained by the self-localization effects. It is likely determined by the spin diffusion length in the Cu layer, but nevertheless thoughtful micromagnetic simulations should be performed. Then, both the phase locking of the NLSI-based oscillators with an external signal and the mutual phase locking are particularly interesting. Finally, for the complete understanding it would be helpful to analyze the magnetization dynamics in the nonlocal oscillators at different out-of-plane angles of the external magnetic field.

This thesis contributed partially to the following publications:

1) V. E. Demidov, S. Urazhdin, **B. Divinskiy**, A. B. Rinkevich and S. O. Demokritov, Appl. Phys. Lett. 107, 202402 (2015).

2) V. E. Demidov, S. Urazhdin, R. Liu, **B. Divinskiy**, A. Telegin and S. O. Demokritov, Nature Communications, 7 , 10446 (2016).

Appendix

COMSOL simulations

Table of material parameters used in the simulations:

	Cu	Py	CoFe	Au	Silicon	Sapphire
Density, kg/m^3	8700	8700	8950	19300	2329	3970
Electrical conductivity, S/m	$1.6 \cdot 10^7$	$2.5 \cdot 10^6$	$4 \cdot 10^6$	$4.1 \cdot 10^7$	$1 \cdot 10^{-12}$	$1 \cdot 10^{-12}$
Thermal conductivity, $W/(m \cdot K)$	400	46.4	29.3	318	130	33
Heat capacity, $J/(kg \cdot K)$	385	430	376	128	700	750
Relative permittivity	1	1	1	1	11.7	10

The resistivity values are specified in the text. All geometrical sizes can be found in [30] and [36]. Mesh was used with maximum element size 1.6 μm and minimum 0.25 nm.

Mumax3 simulations

Mumax3 script which was used to calculate the spin-wave dispertion law in Chapter 6:

```
widthWG := 0.5e-6
thicknessWG := 20e-9
thicknessBase := 5e-9

sizeX := 12e-6
sizeY := 3e-6
sizeZ := thicknessWG + thicknessBase

Nx := 1200
Ny := 150
Nz := 5
SetPBC(5, 0, 0)
SetGridSize(Nx, Ny, Nz)
SetCellSize(sizeX/Nx, sizeY/Ny, sizeZ/Nz)
```

```
a := cuboid(sizeX, widthWG, thicknessWG).transl(0, 0, sizeZ/2-thicknessWG/2)
b := cuboid(sizeX, SizeY, thicknessBase).transl(0, 0, -(sizeZ/2 - thicknessBase/2))
setgeom(a.add(b))

Msat = 780e3
alpha = 1
Aex = 13e-12
m = uniform(0, 1, 0)
Bstat := 1000e-4
B_ext = vector(0, Bstat, 0)
t0 := 10e-9
Run(t0)
saveas(m, "groundstate_m")

N := 0
workalpha := 1e-10
excXsize := sizeX
excYsize := widthWG

alpha = workalpha
Amp := 1e-4
fmax := 20e9
mask := newVectorMask(Nx, Ny, 1)
for i := 0; i < Nx; i++ {
    for j := 0; j < Ny; j++ {
        r := index2coord(i, j, 0)
        x := r.X()
        y := r.Y()
        B := cos(2 * pi * x / excXsize * N)
        if x < (excXsize / 2) {
            if x > (-excXsize / 2) {
                if (y > -excYsize/2) && (y < excYsize/2) {
                    mask.setVector(i, j, 0, vector(B, 0, 0))
                }
            }
        }
     }
}

B_ext.add(mask, Amp*sin(2*pi*fmax*(t-t0))/(2*pi*fmax*(t-t0)))
tableautosave(1e-12)
autosave(m, 0.05e-9)
run(10e-9)
```

Literature

[1] V. V. Kruglyak, S. O. Demokritov, and D. Grundler, J. Phys. D: Appl. Phys. 43, 264001 (2010).

[2] B. Lenk, H. Ulrichs, F. Garbs, and M. Mnzenberg, Physics Reports 507, 107-136 (2011).

[3] A. V. Chumak, V. I. Vasyuchka, A. A. Serga and B. Hillebrands, Nature Phys. 11, 453-461 (2015).

[4] F. Bloch, Zeitschrift fr Physik 61, 206-219 (1930).

[5] A. G. Gurevich, G. A. Melkov, "Magnetitation Oscillations ans Waves", CRC Press (1996).

[6] D. D. Stancil, A. Prabhakar, "Spin Waves: Theory and Applications", Springer (2009).

[7] V.S. L'vov, "Wave Turbulence under Parametric Excitations", Springer Series in Nonlinear Dynamics, 1994.

[8] R. P. Feynman, "Statistical Mechanics: A Set Of Lectures", Westview Press (1998).

[9] Demidov, V. E. et al., Appl. Phys. Lett. 95, 112509 (2009).

[10] V. E. Demidov, S. Urazhdin, A. Zholud, A. V. Sadovnikov and S. O. Demokritov, Appl. Phys. Lett. 106, 022403 (2015).

[11] V. E. Demidov and S. O. Demokritov, IEEE Trans. Mag. 51, 0800215 (2015).

[12] J. C. Slonczewski, J. Magn. Magn. Mater. 159, L1-L7 (1996).

[13] L. Berger, Phys. Rev. B 54, 9353-9358, 1996.

[14] N. Locatelli, V. Cros and J. Grollier, Nature Materials 13, 11 (2014).

[15] D. C. Ralph, M. D. Stiles, JMMM 320, 1190-1216 (2008).

[16] Stephen E. Russek, William H. Rippard, Thomas Cecil and Ranko Heindl, "Spin-Transfer Nano-Oscillators" in "Handbook of Nanophysics: Functional Nanomaterials", edited by Klaus D. Sattler, CRC Press (2010).

[17] M. Tsoi, A. G. M. Jansen, J. Bass, W. C. Chiang, M. Seck, V. Tsoi, and P.Wyder, Phys. Rev. Lett. 80, 42814284 (1998).

[18] M. Tsoi, A. G. M. Jansen, J. Bass, W. C. Chiang, V. Tsoi, and P.Wyder, Nature 406, 4648 (2000).

[19] J. A. Katine, F. J. Albert, R. A. Buhrman, E. B. Myers, and D. C. Ralph, Phys. Rev. Lett. 84, 3149 (2000).

[20] S. I. Kiselev, J. C. Sankey, I. N. Krivorotov, N. C. Emley, R.J. Schoelkopf, R. A. Buhrman, and D. C. Ralph, Nature 425, 380383 (2003).

[21] W. H. Rippard, M. R. Pufall, S. Kaka, S. E. Russek, and T. J. Silva, Phys. Rev. Lett. 92, 027201 (2004).

[22] T.J. Silva and W.H. Rippard, JMMM 320, 1260 - 1271 (2008).

[23] Luqiao Liu, Takahiro Moriyama, D. C. Ralph, and R. a. Buhrman, Phys. Rev. Lett. 106, 036601 (2011).

[24] Luqiao Liu, Chi-Feng Pai, Y. Li, H. W. Tseng, D. C. Ralph, R. A. Buhrman, Science 336, 6081 (2012).

[25] K. Ando, S. Takahashi, K. Harii, K. Sasage, J. Ieda, S. Maekawa, and E. Saitoh, Phys. Rev. Lett. 101, 036601 (2008).

[26] V. E. Demidov, S. Urazhdin, E. R. J. Edwards, M. D. Stiles, R. D. McMichael and S. O. Demokritov, Phys. Rev. Lett. 107, 107204 (2011).

[27] V. E. Demidov, S. Urazhdin, E. R. J. Edwards, and S. O. Demokritov, Appl. Phys. Lett 99, 172501 (2011).

[28] Shinya Kasai, Kouta Kondou, Hiroaki Sukegawa, Seiji Mitani, Kazuhito Tsukagoshi and Yoshichika Otani, Appl. Phys. Lett. 104, 2013-2016 (2014).

[29] V. E. Demidov, S. Urazhdin, H. Ulrichs, V. Tiberkevich, A. Slavin, D. Baither, G. Schmitz, and S. O. Demokritov, Nature Materials 11, 1028 (2012).

[30] V. E. Demidov, S. Urazhdin, A. Zholud, A. V. Sadovnikov, and S. O. Demokritov, Appl. Phys. Lett. 105, 172410 (2014).

[31] Z. Duan, A. Smith, L. Yang, B. Youngblood, J. Lindner, V. E. Demidov, S. O. Demokritov, and I. N. Krivorotov, Nat. Commun. 5, 5616 (2014).

[32] T. Kimura, Y. Otani, and J. Hamrle, Phys. Rev. Lett. 96, 037201 (2006).

[33] Tao Yang, Takashi Kimura, and Yoshichika Otani, Nature Physics, 4(11), 851-854 (2008).

[34] Lin Xue, Chen Wang, Yong-Tao Cui, Luqiao Liu, A. Swander, J. Z. Sun, R. A. Buhrman, and D. C. Ralph1, Phys. Rev. Lett. 108, 147201 (2012).

[35] P. S. Keatley, A. Aziz, M. Ali, B. J. Hickey, M. G. Blamire, and R. J. Hicken, PRB 89, 094421 (2014).

[36] V. E. Demidov, S. Urazhdin, A. Zholud, A. V. Sadovnikov, A. N. Slavin, and S. O. Demokritov, Sci. Rep. 5, 8578 (2015).

[37] L.D. Landau, E.M. Lifshitz, Phys. Z. Sowietunion 8, 153 (1935).

[38] Prof. Dr. Sergej Demokritov and Dr. V. E. Demidov, lectures "Einführung in die Magnonik" at Westfälische Wilhelms-Universität Münster (2014).

[39] Gavin S. Abo , Yang-Ki Hong , Jihoon Park , Jaejin Lee , Woncheol Lee , and Byoung-Chul Choi, IEEE Transactions on Magnetics 49, 4937-4939 (2013).

[40] K. Y. Guslienko, V. Novosad, Y. Otani, H. Shima, and K. Fukamichi, Phys. Rev. B 65 (2), 024414 (2001).

[41] J. A. Osborn, Phys. Rev. 67, 351 (1945).

[42] R. I. Joseph, E. Schlomann, J. Appl. Phys. 36, 1579 (1965).

[43] J. C. Slonczewski, J. Magn. Magn. Mater. 195, L261-L268 (1999).

[44] Andrew D. Kent and Daniel C. Worledge, Nature Nanotechnology 10, 187 (2015).

[45] A. Jenkins, arXiv:1109.6640.

[46] A. Slavin and V. Tiberkevich, IEEE Trans. Mag. 45, 1875 (2009).

[47] A. Slavin and V. Tiberkevich, IEEE Trans. Magn. 44, 19161927 (2008).

[48] A. Slavin and P. Kabos, IEEE Trans. Magn. 41, 12641273 (2005).

[49] M. I. Dyakonov and V. I. Perel, JETP Lett. 13, 467-469 (1971).

[50] J. E. Hirsch, Phys. Rev. Lett. 83, 1834-1837 (1999).

[51] A. Hoffman, IEEE Trans. Magn. 49 (2013).

[52] M. I. Dyakonov, arXiv:1210.3200.

[53] J. Sinova, S. O. Valenzuela, J. Wunderlich, C. H. Back and T. Jungwirth, Rev. Mod. Phy. 87 (2015).

[54] V.E. Demidov, H. Ulrichs, S.V. Gurevich, S.O. Demokritov, V.S. Tiberkevich, A.N. Slavin, A. Zholud, and S. Urazhdin, Nat. Commun. 5, 3179 (2014).

[55] H. Ulrichs, V. E. Demidov, and S. O. Demokritov, Appl. Phys. Lett. 104, 042407 (2014).

[56] A. Hamadeh, O. dAllivy Kelly, C. Hahn, H. Meley, R. Bernard, A. H. Molpeceres, V. V. Naletov, M. Viret, A. Anane, V. Cros, S. O. Demokritov, J. L. Prieto, M. Muoz, G. de Loubens, and O. Klein, Phys. Rev. Lett. 113, 197203 (2014).

[57] S. O. Demokritov and V. E. Demidov, IEEE Trans. Mag. 44, 1 1 (2008).

[58] Henning Ulrichs, PhD thesis "Spin-wave instabilities on the nanoscale", Westf"alische Wilhelms-Universit"at M"unster, 2014.

[59] Production of JRS Scientific Instruments, Switzerland.

[60] M. G. Cottam and D. J. Lockwood, "Light Scattering in Magnetic Solids", Wiley-Interscience Publication (1986).

[61] M.J. Donahue and D.G. Porter, OOMMF User's Guide, Version 1.0.

[62] A. Vansteenkiste, J. Leliaert, M. Dvornik, M. Helsen, F. Garcia-Sanchez and B. Van Waeyenberge, AIP Advances 4, 107133 (2014).

[63] R. D. McMichael and M. D. Stiles, Journal of Applied Physics 97, 10J901 (2005).

[64] COMSOL Multiphysics software from COMSOL, Inc.

[65] Yi Liu, Zhe Yuan, R. J. H. Wesselink, Anton A. Starikov, and Paul J. Kelly, Phys. Rev. Lett. 113, 207202 (2014).

[66] C. Kittel, Phys. Rev. 73, 155 (1948).

[67] B. A. Kalinikos, IEE Proc. H 127, 4-10 (1980).

[68] B. A. Kalinikos and A. N. Slavin,J. Phys. C, Solid State Phys. 19 (35), 70137033 (1986).

Acknowledgments

First of all, I would like to thank Prof. Dr. Sergej Demokritov for the possibility to be a part of his group and general guidance during my studies. I am also very grateful to Dr. Vladislav Demidov for fruitful discussions about magnetization dynamics and experimental methods. I thank other members of the group "Nonlinear Magnetic Dynamics" for a positive work environment.

I would like to specially thank PD Dr. Sergej Divinski and his family for their kindness and support during my stay in Germany.

Last but not least I would like to thank all my family, especially my parents. For everything.

Plagiatserklarung

Hiermit versichere ich Boris Divinskiy, dass die vorliegende Arbeit mit dem Titel "Study of spin-torque nano-oscillators driven by nonlocal spin injection" selbstständig verfasst worden ist, dass keine anderen Quellen und Hilfsmittel als die angegebenen benutzt worden sind und dass die Stellen der Arbeit, die anderen Werken - auch elektronischen Medien - dem Wortlaut oder Sinn nach entnommenen wurden, auf jeden Fall unter Angabe der Quelle als Entlehnung kenntlich gemacht worden sind.

_____

Münster, 07.03.2016

Ich erkläre mich mit einem Abgleich der Arbeit mit anderen Texten zwecks Auffindung von Übereinstimmungen sowie mit einer zu diesem Zweck vorzunehmenden Speicherung der Arbeit in eine Datenbank einverstanden.

_____

Münster, 07.03.2016